Acta Materialia 264 (2024) 119566

Contents lists available at ScienceDirect

Acta Materialia

journal homepage: www.elsevier.com/locate/actamat

Effect of deformation temperature on strain localization phenomena in an austenitic Fe-30Mn-6.5Al-0.3C low-density steel

Ivan Gutierrez-Urrutia *, Akinobu Shibata

Research Center for Structural Materials, National Institute for Materials Science (NIMS), 1-2-1, Sengen, Tsukuba 305-0047, Japan

ARTICLE INFO

Keywords:
Strain localization
Fe-Mn-Al-C low-density steel
Austenitic steels
Strain-hardening
Electron channeling contrast imaging (ECCI)

ABSTRACT

We have investigated the influence of the deformation temperature from 25 °C (RT) to -196 °C on the dislocation structures associated with strain localization phenomena in an austenitic Fe-30Mn-6.5Al-0.3C (wt.%) low-density steel by electron channeling contrast imaging (ECCI), electron backscatter diffraction (EBSD), and bright-field transmitted forescattered electron imaging ((BF) t-FSEI) techniques. The characteristics of the dislocation structures were evaluated on the main texture components, i.e. <111>//tensile axis, <112>//tensile axis, and <001>//tensile axis directions. The inhomogeneous character of the plastic behavior is promoted upon cryogenic deformation due to the formation of dislocation structures associated with strain localization, namely microbands (MBs) and deformation bands (DBs). ECCI analysis of the dislocation structure reveals that the deformation temperature has a strong influence on the thermal-assisted dislocation processes controlling the dislocation configurations and MB formation mechanisms. The MB nucleation mechanism evolves from a cross-slip-assisted mechanism at RT deformation conditions to a slip band-assisted mechanism at cryogenic deformation temperatures. This effect has a profound effect on the grain orientation dependence of the MB structure but not on its crystallographic alignment. On the other hand, cryogenic deformation temperatures (-196 °C) enhance the material's mechanical strength and ductility due to the activation of deformation twinning, which is associated with the reduction of the stacking fault energy. We find that MBs have a small contribution to strain-hardening and ductility due to the small mechanical resistance of these dislocation structures against the advance of deformation twins and dense dislocation layers, and the comparatively small plastic strain accommodated by them, respectively. These findings provide new insights into the microband-induced plasticity (MBIP) effect.

1. Introduction

The inhomogeneous plastic deformation associated with strain localization phenomena has received much attention due to its influence on the deformation behavior of novel austenitic (fcc, face-centered cubic) multicomponent alloys such as FeMnAlC low-density steels [1–9], FeNiMnAlCr high-entropy alloys [10,11], NiCoFeCrMoW high-entropy alloys [12], and CoCrFeMnSi high-entropy alloys [13,14]. Strain localization phenomena are associated with local shear instabilities on the deformation structure resulting in the formation of characteristic deformation structures such as microbands (MBs) and shear bands (SBs) that propagate through the material. SBs are non-crystallographic band-like regions characterized by a massive collective dislocation activity concentrated in a narrow local deformation zone that is surrounded by a matrix that undergoes comparably homogenous deformation [15–18]. MBs are in-grain band-like regions formed by paired dense dislocations layers with a thickness of ~ 100 - 200 nm [1]. From a deformation standpoint, SBs are associated with intense plastic localization resulting in large rotations (20 - 30°) of the crystal lattice with respect to the surrounding matrix. On the other hand, small lattice rotations (< 5°) are accommodated by MBs due to the moderated plastic strain associated with them. Strain localization phenomena play a relevant role in mechanical properties such as ductility [19–23] and mechanical anisotropy upon strain path changes [24,25]. In austenitic FeMnAlC low-density steels, several studies have suggested that MB formation results in an enhanced plastic behavior, the so-called microband-induced plasticity (MBIP) effect [2–4,9]. This effect can provide enhanced plasticity to materials that undergo significant strain localization. However, the details of the underlying mechanism associated with MBIP as well as the contribution of MBs to the strain-hardening behavior are still unclear [1–3,6,7,10,11,13]. Recently, we have investigated the deformation structures associated with strain

* Corresponding author.
E-mail address: gutierrezurrutia.Ivan@nims.go.jp (I. Gutierrez-Urrutia).

https://doi.org/10.1016/j.actamat.2023.119566
Received 10 August 2023; Received in revised form 26 November 2023; Accepted 30 November 2023
Available online 2 December 2023

localization phenomena in a Fe-30Mn-6.5Al-0.3C (wt.%) low-density steel deformed at −196 °C [8]. This study shows that the strain level plays a relevant role in the activation of the MB nucleation mechanisms. Specifically, at moderated strain levels (ε = 0.3), the dominant MB nucleation mechanism is associated with localized planar slip phenomena acting on closely spaced slip bands. At high strain levels (ε = 0.6), a grain boundary-assisted MB nucleation mechanism is activated together with the development of macroscopic deformation bands (DBs) containing arrays of MBs. Due to the current interest in austenitic FeMnAlC low-density steels as structural materials for a wide range of application temperatures from room temperature to cryogenic temperatures [5,26,27], the investigation of the influence of the deformation temperature on strain localization phenomena can provide further insight into the deformation behavior of these materials. In particular, the analysis of the dislocation-based processes controlling the formation of the dislocation structures associated with strain localization phenomena can provide further understanding to their contribution to plasticity.

The present study aims to understand the influence of the deformation temperature from 25 °C to −196 °C on the deformation structures associated with strain localization phenomena in an austenitic Fe-30Mn-6.5Al-0.3C (wt.%) low-density steel. In particular, we focus on the effect of the deformation temperature on the dislocation processes that control the nucleation mechanisms of the dislocation structures associated with strain localization, such as microbands and deformation bands. The most relevant characteristics of these deformation structures were quantitatively analyzed in the main texture components, namely <111>//tensile axis, <001>//tensile axis, and <112>//tensile axis directions, by the combination of the electron channeling contrast imaging (ECCI) and electron backscatter diffraction (EBSD) techniques. The contribution of these deformation structures to the deformation behavior, strain-hardening, and ductility is quantitatively analyzed.

2. Materials and methods

The low-density steel investigated in the present study had the chemical composition Fe-30Mn-6.5Al-0.3C (wt.%). Details of material processing can be found in [8]. The annealed material contains a fully austenitic structure with an average grain size of 175 μm, which remained stable between −196 °C and 25 °C. Cylindrically shaped specimens of 6 mm in diameter and 30 mm in gage length were machined by spark erosion from the rolled plates along the rolling direction. The geometry of the tensile samples is depicted in Fig. 1. Tensile tests were carried out at an initial strain rate of 5.6×10^{-4} s^{-1} in a Shimadzu AGX tensile machine equipped with a liquid nitrogen bath. The deformation structure associated with strain localization phenomena was evaluated in grains oriented on the main texture components along the line between the <001>//TA and <111>//TA crystallographic directions (TA: tensile axis) at engineering strains of ε = 0.3 and ε = 0.5 - 0.6. The crystallographic alignment of the dislocation configurations was evaluated by the EBSD-ECCI trace analysis approach described in [8]. The deformation structure was characterized by several scanning electron microscope (SEM) techniques, namely, electron backscatter diffraction (EBSD), bright-field transmitted forescattered electron imaging ((BF) t-FSEI), and electron channeling contrast imaging (ECCI). The SEM techniques were performed in a Sigma Zeiss FEG-SEM (Carl Zeiss SMT AG, Germany) that is equipped with a TSL Orientation Imaging Microscopy (OIM) EBSD system. The observation direction was perpendicular to the tensile axis. EBSD measurements were performed at 20 kV acceleration voltage, 15 mm working distance, and a step size of 100 nm. ECCI was conducted at 20 kV using a solid-state four-quadrant backscatter electron (BSE) detector at a 5 – 6 mm working distance. The microscope was run in the high-current mode. ECC images were acquired by the EBSD-based ECCI approach described in [28,29]. ECC images of individual dislocations were taken with optimum contrast under channeling conditions with large positive values of w (w: deviation parameter), as described in [30]. The apparent values of dislocation boundary spacings and sizes of dislocation configurations measured on ECC images were corrected by a stereological correction considering the specific tilting conditions. ECCI samples were mechanically polished with 800 and 1200 SiC grit papers and subsequently polished with 3 and 1 μm diamond suspensions. Final polishing was performed with 50 nm colloidal silica suspension. Tilting experiments were carried out on a 5-axis motorized eucentric stage (x, y, z, tilt, rotation) with x/y/z step resolution of 1 μm and tilt/rotation step resolution of 0.1°. (BF) t-FSEI was conducted at 30 kV using an on-axis transmission Kikuchi Diffraction (TKD) system that consists of a Bruker e^{-}Flash^{HD} EBSD (Bruker, Billerica, MA, USA) camera mounted on a Bruker OPTIMUS TM detector head. The detector head consists of a phosphor screen and three forescattered electron detectors (FSD) with a size of 5.2 × 4.4 mm^2 for collecting the transmission forescattered electron (t-FSE) signal produced within the sample. (BF) t-FSE images were acquired by placing the FSD normal to the optic axis beneath the sample, as described in [31]. TEM analysis was performed in a JEOL JEM 2800 TEM operating at 200 kV. Before imaging, the TEM sample was plasma-cleaned using an XEI Evactron 25 (XEI Scientific, Inc., Redwood City, USA) de-contaminator. TEM and t-FSEI samples were fabricated by using the in-situ FIB lift-out method on a Scios 2 ThermoFisher Scientific dual-beam SEM system at an acceleration voltage of 30 kV and a Ga^{+} current of ~1000 pA on both sides of the foil followed by a final thinning procedure at 5 kV and 200 pA. The size of the lamella fabricated by FIB was about 20 μm × 20 μm × 100 nm.

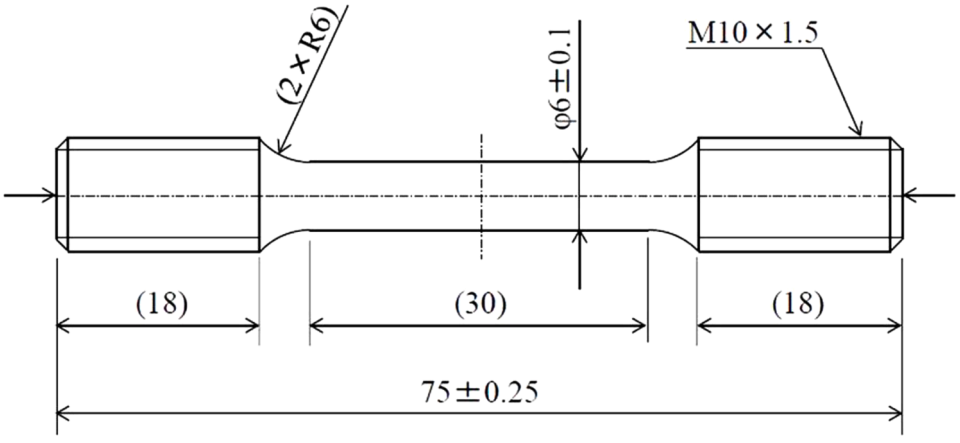

Fig. 1. Drawing of the shape and dimensions of the cylindrical specimens used for tensile testing (dimensions are in mm).

3. Results

3.1. Mechanical behavior

Fig. 2 shows the engineering tensile stress-strain curves (a) and true stress-strain curves (b) of the specimen tensile deformed at the deformation temperatures of 25 °C (RT), −100 °C, and −196 °C. The mechanical data are summarized in Table 1. The plot shows that the deformation temperature has a significant influence on mechanical behavior. With the decrease of the deformation temperature, yield stress (YS), ultimate tensile strength (UTS), uniform elongation (UEL), and total elongation (TEL) significantly increase. However, whereas the UTS, UEL, and TEL only increase at the deformation temperature of −196 °C, YS steadily increases within the range of low-temperature deformation. The mechanical data indicate that the strengthening mechanisms controlling YS (e.g. solute strengthening and Taylor hardening) are more sensitive to the deformation temperature than the mechanical properties (UTS, UEL, TEL) associated with the deformation structure. These effects have been previously reported in austenitic FeMnAlC low-density steels where the austenite phase is mechanically stable (i.e. no martensitic transformation is induced) [5,32,33].

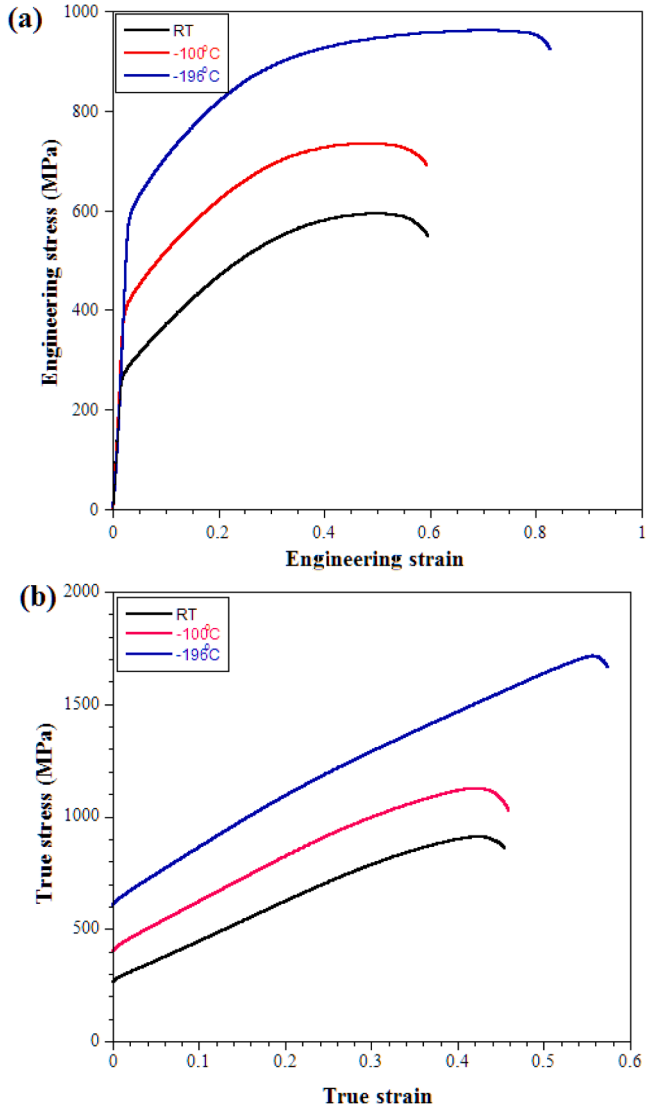

Fig. 2. Engineering tensile stress-strain curves (a) and true stress-strain curves (b) of the Fe-30Mn-6.5Al-0.3C low-density steel at the deformation temperatures of 25 °C (RT), −100 °C, and −196 °C.

Table 1
Mechanical properties of the Fe-30Mn-6.5Al-0.3C low-density steel tensile deformed at the deformation temperatures of 25 °C (RT), −100 °C, and −196 °C. YS: Yield strength; UTS: ultimate tensile strength; UEL: uniform elongation; TEL: elongation to fracture.

Deformation temperature	YS (MPa)	UTS (MPa)	UEL	TEL
RT	270 ± 10	496 ± 10	0.51	0.65
−100 °C	400 ± 10	498 ± 10	0.52	0.65
−196 °C	590 ± 20	715 ± 20	0.78	0.85

3.2. Evolution of the room-temperature deformation structure

3.2.1. Moderated strain level ($\varepsilon = 0.3$)

Figs. 3-5 show the room-temperature (RT) deformation structures formed at $\varepsilon = 0.3$ of grains oriented close to <111>//TA directions. Specifically, Fig. 3 shows the RT deformation structure of a grain oriented close to the [9 8 12]//TA direction. It consists of a microband (MB) structure formed by two systems that are aligned parallel to {315} plane traces, i.e. the alignment is non-crystallographic. The MB structure subdivides the grain into blocks with an MB spacing, λ_{MB}, ranging between 5 and 10 μm. The KAM-EBSD map of Fig. 3(b) shows that MBs are associated with moderated lattice rotations (misorientation angles of 2 - 3° with respect to the surrounding crystal matrix are estimated from EBSD) that are accommodated by geometrically necessary dislocations. As shown in the ECC image of Fig. 3(c), MBs consist of plate-like structures with an average thickness of 220 ± 20 nm that propagate through the grain interior. Under the current (−220) channeling conditions, the MB plate is imaged in an out-of-Bragg condition and hence, it is visible as a bright plate over a dark background.

To analyze the MB formation mechanisms, we have evaluated the dislocation configuration of the crystal matrix in an area containing MBs (Fig. 4). As the ECC image of Fig. 4(a) reveals, a high density of dislocations ($\rho \sim 4.5 \pm 0.5 \times 10^{14}$ m^{-2}) with wavy character are formed in the grain interior. The average dislocation density was estimated using the relationship $\rho = 2\,N/Lt$, where N is the number of dislocation lines intersecting a grid of total line length L on the ECC image, and t is the ECCI probe depth [34] (under the current microscope conditions, $t \sim 75$ nm [35]). Combined ECCI and EBSD analysis shows that the dislocation lines of the wavy dislocations are aligned along the [1 1 0], [0 1 −1], and [−1 1 0] directions. These dislocation line directions correspond to those of the primary slip plane (1 −1 1) [0 1 1], and the cross-slip planes (1 1 1) [0 1 −1] and (1 1 1) [−1 1 0], respectively. As an example, the dislocation line directions of a wavy dislocation with a segment that cross-slipped onto the cross-slip system (1 1 1) [−1 1 0] are indicated in Fig. 4(a).

Fig. 4(c) shows the variation of the BSE intensity along the dislocation line indicated in Fig. 4(b). It can be seen that the BSE intensity is nearly constant along the dislocation line. This contrast behavior is unusual for the present inclined dislocation configuration since the contrast intensity tends to be attenuated along the dislocation line that is located further away from the sample surface [36,37]. The observed dislocation contrast is consistent with that of inclined edge dislocation dipoles observed in fcc metals, which is associated with the channeling contrast formed by dislocation kinks distributed along the dislocation lines of edge dislocation dipoles [38–40]. Interestingly, in regions close to the grain boundaries of grains oriented close to <111>//TA directions, arrays of edge dipole bundles propagating towards the grain interior were observed. Fig. 5 shows an example of the propagation of arrays of edge dipole bundles in a region of the grain G1 (oriented close to the [9 8 12]//TA direction) that is close to the grain boundary G1 – G2. The ECC images (b, c) were taken under (−2 2 0) channeling conditions with $w >> 0$. It can be seen that the bundles are formed by a high density of closely spaced dipoles with a spacing of ~ 10 nm. As Fig. 5(c) shows, the dipoles exhibit the characteristic constant contrast along the dislocation line observed in Fig. 4.

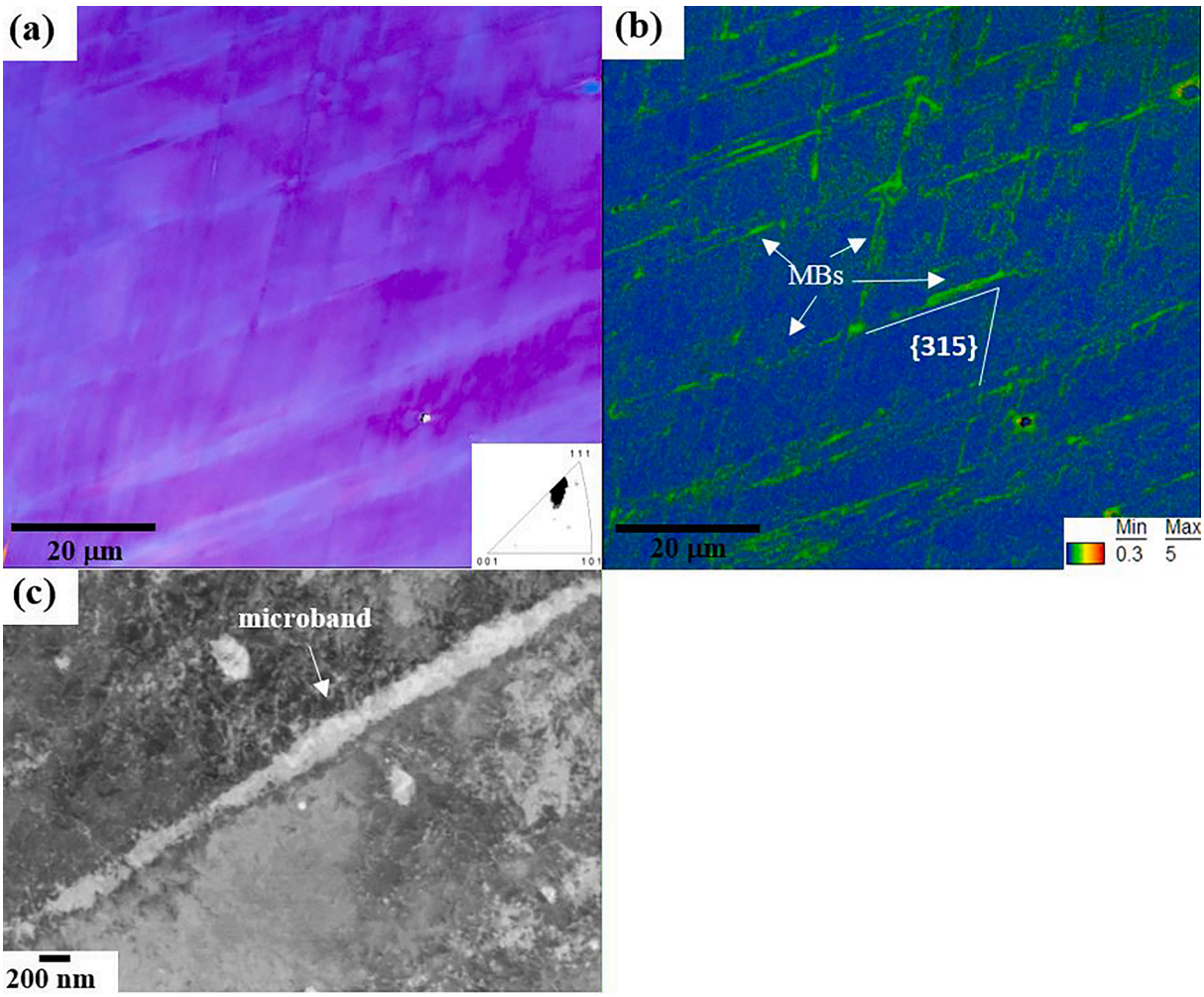

Fig. 3. Microband (MB) structure formed at RT tensile deformation conditions ($\varepsilon = 0.3$) of a grain oriented close to the [9 8 12]//TA direction. (a): IPF-EBSD map; (b): KAM-EBSD map; (c): ECC image of a microband formed in the area imaged in (a, b). The ECC image was taken under (−220) channeling conditions.

At this deformation stage, the dislocation structures of grains oriented close to <112>//TA and <001>//TA directions are formed by a regular distribution of cell blocks (CBs) and dislocation cells (DCs), respectively. Fig 6(a, b) show the CB structure of a grain oriented close to the [3 2 10]//TA direction. The structure consists of lamellar CBs that are aligned parallel to {315} plane traces (angle deviation < 5°). As shown in the ECC image of Fig. 6(b), CBs consist of in-grain shearing structures with a lamellar morphology with an average thickness of 300 ± 50 nm. The ECC image was taken under (2 1 −1) channeling conditions where the CBs are imaged in an out-of-Bragg condition. Fig. 6(c) shows the DC structure of a grain oriented close to the [3 1 26]//TA direction. The estimated average DC size is 280 ± 20 nm. The ECC image was taken under (0 2 0) channeling conditions.

3.2.2. *High strain level ($\varepsilon = 0.5$)*

With further deformation ($\varepsilon = 0.5$), the main characteristics of the RT deformation structure are the formation of a deformation twin structure in grains oriented close to <111>//TA directions (Fig. 7) and the formation of MBs ascribed to the activation of grain boundary-assisted MB nucleation in grains oriented close to <001>//TA and <112>//TA directions (Fig. 8). The activation of deformation twinning is controlled by the twinning stress, σ_{tw}, which is given as $\sigma_{tw} = \gamma_{SFE}/bm$, where γ_{SFE} is the stacking fault energy, m is the Schmid factor for twinning, and b is the Burgers vector [41]. Assuming $\gamma_{SFE} = 78 \pm 10$ mJ/m^2 (estimated from a modified Olson–Cohen thermodynamical model [8,42,43] and using the data available for the Fe-Mn-Al-C system [44–47]), m ~ 3.06, and $b = 2.5 \times 10^{-10}$ m, we obtain $\sigma_{tw} = 830$ - 1075 MPa. This stress range corresponds to a true strain (ε_t) range of $\varepsilon_t = 0.33 – 0.45$ (engineering strain, ε, range of 0.4 – 0.57). The highest true strain value ($\varepsilon_t = 0.45$) corresponds to that of the true fracture stress. This finding indicates that deformation twinning at RT deformation conditions is activated at the later stages of deformation. Fig. 7 shows the deformation structure of a grain oriented close to the [7 7 8]//TA direction. The deformation structure consists of an inter-connected MB and twin structure (Fig. 7(a, c)) together with a DC structure (Fig. 7(d)). As suggested by the pioneering studies of Kuhlmann-Wilsdorf [48–50], the mechanically unstable dipole configurations formed at early deformation stages, such as those shown in Fig. 4, evolve into a DC structure to minimize the energy of the dislocation configuration. The process involves the activation of dislocation reaction products formed by the interaction of secondary slip with the primary edge dislocations. The MB structure consists of two non-coplanar systems, namely, MB1 and MB2. The MBs are associated with the activation of highly stressed slip systems, namely, (1 −1 1) [0 −1 −1] and (1 −1 1) [1 1 0] slip systems (MB1), and (−1 1 1) [1 0 1] and (−1 1 1) [−1 −1 0] slip systems (MB2). The twinning structure is formed by two twinning systems with high Schmid factors (SFs), namely (1 −1 1) [1 2 1] with SF = 0.34 (TW1), and (1 1 −1) [1 1 2] with SF = 0.26 (TW2). The analysis reveals that MB1 is activated on the same plane as TW1, i.e. (1 −1 1). However, they are not activated at the same location. Deformation twins are nucleated at a GB (not visible in Fig. 7) and propagate through the grain interior until the nearest GB. MBs are nucleated in the grain interior induced by strain

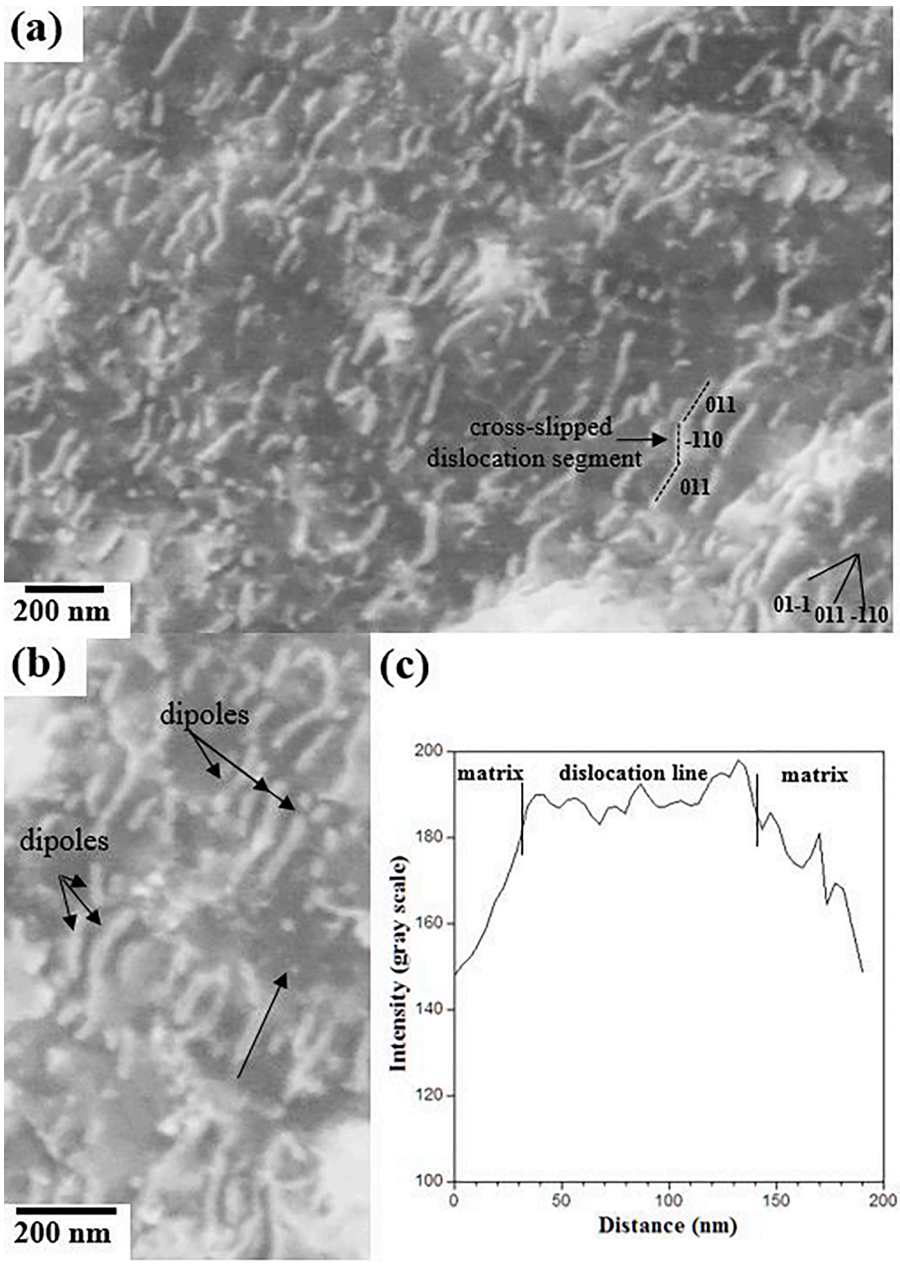

Fig. 4. (a): ECC image of the dislocation configuration in the crystal matrix of an area containing microbands (MBs) formed at RT tensile deformation conditions ($\varepsilon = 0.3$). The grain is oriented close to the [9 8 12]//TA direction. The ECC image was taken under (−220) channeling conditions with $w >> 0$. (b-c): Analysis of the channeling contrast corresponding to dipoles. The contrast intensity profile plotted in (c) corresponds to that along the dislocation line indicated by an arrow in (b).

localization phenomena (Section 4.2). Interestingly, MBs and DCs are sheared by deformation twins (TW) resulting in a decrease in the overall average boundary spacing (indicated by arrows in Fig. 7(c)).

Fig. 8 shows an example of the grain boundary-assisted nucleation of MBs in a grain oriented close to the [1 1 28]//TA direction (G1). MBs are triggered by the local shear stress concentrations produced by the impingement of deformation twins formed in grain G2 on the G1 – G2 grain boundary. The KAM-EBSD map of Fig. 8(b) shows that deformation twins (TW) generate intense local plastic deformation at loci where they impinge on the G1 - G2 grain boundary. Misorientation angles of 2 - 3° of the MB interior with respect to the surrounding crystal matrix are calculated from EBSD. The GB stress concentrations activate the formation of localized MBs in G1 that propagate ~ 30 μm through the grain interior. This strain localization phenomenon has been observed on the Fe-30Mn-6.5Al-0.3C low-density steel deformed at cryogenic deformation temperatures [8].

3.3. Evolution of the deformation structure formed at cryogenic deformation temperatures (−100 °C and −196 °C)

3.3.1. Moderated strain level ($\varepsilon = 0.3$)

Fig. 9 shows an example of the deformation structure of a grain oriented close to <111>//TA directions formed during tensile deformation at −100 °C to $\varepsilon = 0.3$. The deformation structure consists of an inter-connected MB and twin structure formed by highly-stressed MB and twin systems, namely MB1, MB2, TW1, TW2, and TW3. Similar to the RT deformation conditions, these deformation modes correspond to highly stressed twin and MB systems. Interestingly, Fig. 9(c) reveals that the propagation of deformation twins activated on the secondary TW3 system within the grain interior results in the shearing of the existing MB structure. This observation suggests that the secondary twins TW3 are activated after the activation of the MB1 system. With the further decrease of the deformation temperature to −196 °C, the populations of

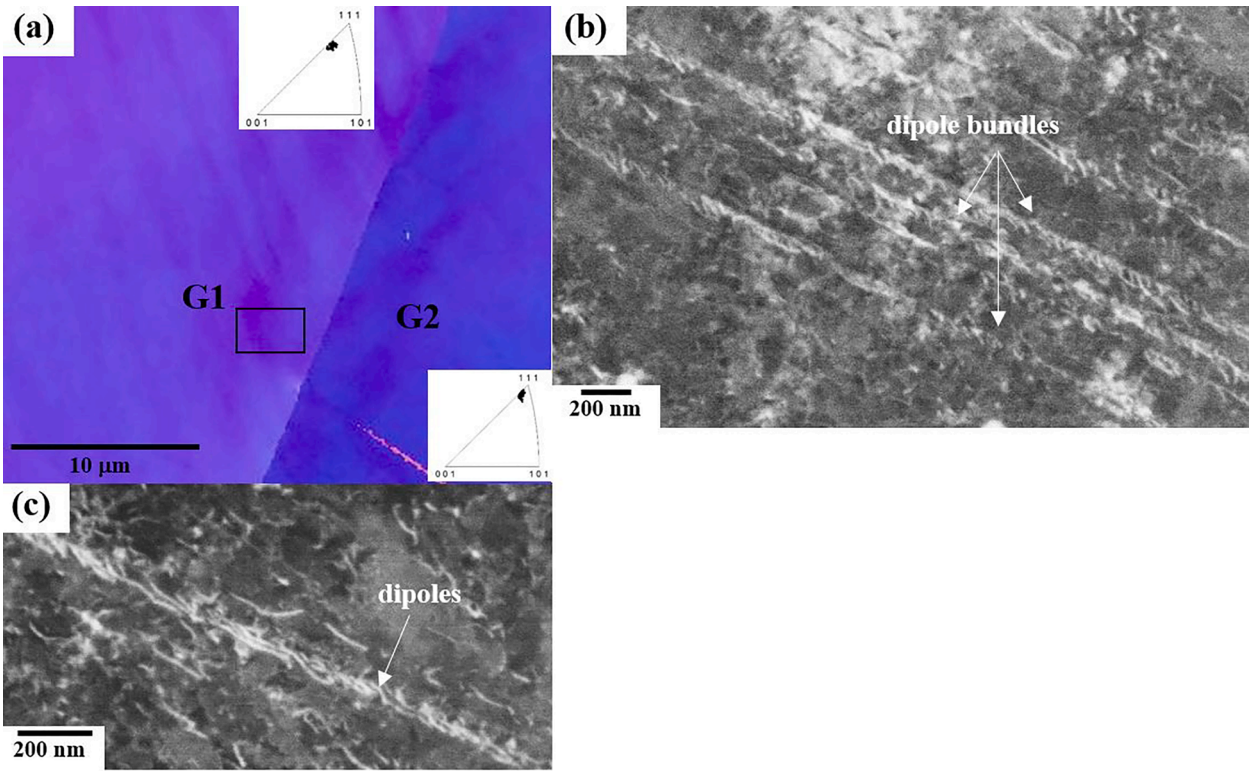

Fig. 5. Propagation of arrays of edge dislocation bundles in a region close to the grain boundary between a grain oriented close to the [9 8 12]//TA direction (G1) and a grain oriented close to the [11 10 13]//TA direction (G2). RT tensile deformation conditions ($\varepsilon = 0.3$). (a): IPF-EBSD map. (b, c): ECC images taken under (−220) channeling conditions with $w >> 0$.

both MBs and deformation twins increase in grains oriented close to <111>//TA directions. Specifically, the average MB spacing, λ_{MB}, is reduced from ~ 2.5 μm at −100 °C to ~ 2.1 μm at −196 °C. This effect indicates that the contribution of strain localization phenomena to the deformation behavior of the Fe-30Mn-6Al-0.3C low-density steel is enhanced upon cryogenic deformation temperatures. The enhanced activity of deformation twinning at −196 °C is ascribed to the reduced σ_{tw}. At cryogenic deformation temperatures, the activation of deformation twinning occurs at low strain levels due to the reduction of γ_{SFE} from 78 ± 10 mJ/m^2 (RT) to 62 ± 10 mJ/m^2 (−100 °C), and 50 ± 10 mJ/m^2 (−196 °C). The values of γ_{SFE} at cryogenic temperatures were predicted using the low-temperature correction from [33]. Specifically, the estimated twinning stresses are σ_{tw} = 635 - 880 MPa (−100 °C) and σ_{tw} = 500 – 735 MPa (−196 °C), which correspond to the true strain (ε_t) ranges of ε_t = 0.10 – 0.23 (engineering strain, ε, of 0.11 – 0.26) and $\varepsilon_t < 0.05$, respectively. The effect of the cryogenic deformation temperature on the twin structure is quantitatively analyzed in Section 3.3.2.

Fig. 10 shows examples of the deformation structures of grains oriented close to the <112>//TA directions formed after tensile deformation at −100 °C to $\varepsilon = 0.3$. The deformation structure consists of lamellar CBs and macroscopic deformation bands (DBs) that are aligned parallel to {315} plane traces (angle deviation < 5°). The CB structure (Fig. 10(a)) contains the same lamellar morphology as that formed at RT deformation conditions. The size of the CB structure formed at cryogenic deformation conditions is similar to that formed at RT deformation conditions (average CB thickness at RT ~ 300 ± 50 nm; average CB thickness at cryogenic deformation temperatures ~ 260 ± 50 nm). Interestingly, DBs were only observed at cryogenic deformation conditions. These macroscopic structures (average thickness ~ 2 μm) are formed in areas containing a high density of closely spaced slip bands and propagate within several grains. Fig. 10(b) shows a (BF) t-FSE image of a DB formed at the deformation temperature of −100 °C. The DB propagates through grains G1 (oriented close to the [12 13 11]//TA direction) and G2 (oriented close to the [3 2 7]//TA direction). The (BF) t-FSE image was taken using the diffraction vector (2 1 −1) under $w >$ 0 diffraction conditions. At the current uniaxial deformation condition, the slip systems with the highest SFs correspond to (1 −1 1) [0 1 1] (SF = 0.47), (−1 1 1) [−1 0 −1] (SF = 0.40), (1 1 1) [0 1 −1] (SF = 0.40) and (1 1 1) [−1 0 1] (SF = 0.32). The (BF) t-FSE image reveals that the boundaries of the DB are formed by localized arrays of highly dense dislocations lying along highly stressed (1 −1 1) and (1 1 1) plane traces. Under the current (2 1 −1) diffraction conditions, [0 1 1] dislocations are not visible. Accordingly, the highly dense dislocations are formed by the activation of the slip systems (1 1 1) [0 1 −1] and (1 1 1) [−1 0 1], which are highly stressed. The boundaries of the DB contain a misorientation of 1.5 – 2.5° (estimated by t-EBSD) with respect to the surrounding crystal matrix, which indicates the occurrence of an intense plastic localization phenomenon. Interestingly, the interaction of dense dislocation layers (DDLs) that propagate through the crystal matrix results in the shearing of the boundaries of the DB. These shearing events produce shear offsets on the boundaries of the DB, as indicated in the ECC image of Fig. 10(c). It is interesting to note that the channeling contrast of DDLs formed in the ECC image of Fig. 10(c) is reverted to that shown on the corresponding (BF)-tFSE image (Fig. 10(b)) [31].

To further understand the plastic mechanism associated with the strain localization observed at the boundaries of the DB, the lattice rotations associated with the deformation structure were analyzed. Fig. 10 (d) plots the rotation axes for misorientations between points in the interior of the DB and neighboring points of the crystal matrix (red dots) and between points in the boundary of the DB and neighboring points of the crystal matrix (blue dots) calculated from misorientation profiles of lines crossing the DB. The plot shows that the interior of the DB is associated with lattice rotations along the line between [0 1 1]//TA and [0 0 1]//TA directions. These lattice rotations are the result of the operation of two equivalent {1 1 1} ⟨1 1 0⟩ slip systems [51]. In particular, the [0 1 1] rotation axis is determined by the direction of the

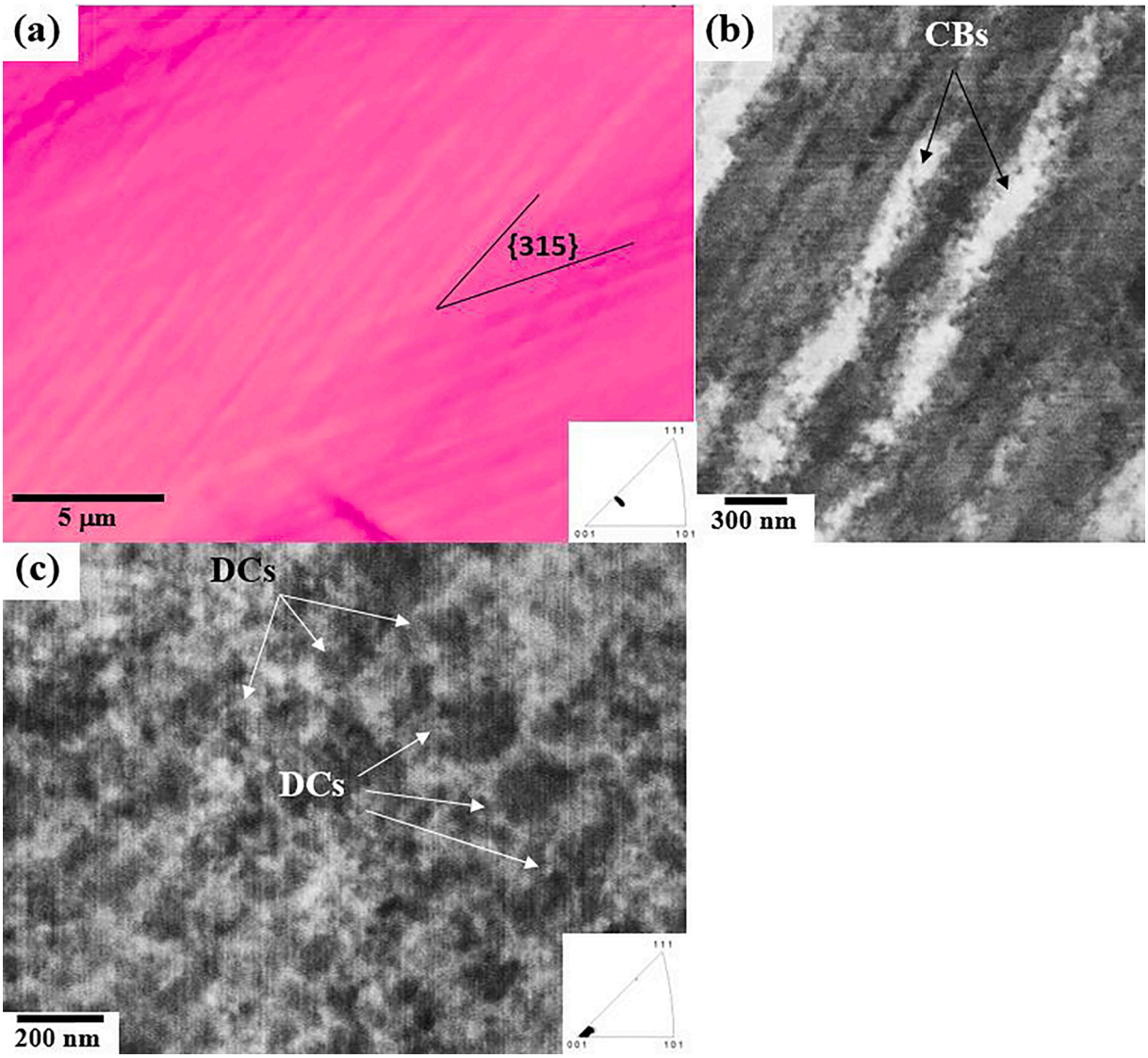

Fig. 6. Room-temperature deformation structures ($\varepsilon = 0.3$) of a grain oriented close to the [3 2 10]//TA direction (a, b) and [3 1 26]//TA directions (c). (a): IPF-EBSD map; (b, c): ECC images of the cell block (CB) and dislocation cell (DC) structures. The ECC images were taken under (−220) and (21–1) channeling conditions, respectively.

slip system with the highest Schmid factor, i.e. (1 −1 1) [0 1 1]. The boundaries of the DB are associated with lattice rotations about [1 1 2]//TA directions. They are the result of the dominant role of the highly stressed (1 −1 1) [0 1 1] slip system. In fcc metals, lattice rotations about [1 1 2]//TA directions have been associated with the formation of deformation structures induced by plastic localization phenomena such as shear bands and MBs where one of the two initially equivalent coplanar slip systems controls the slip behavior [51–53]. These findings indicate that the plastic mechanism associated with the formation of the boundaries of the macroscopic DB corresponds to a plastic localization phenomenon similar to that producing in-grain MBs.

Fig. 11 shows a TEM analysis of an area containing a DB delimited by MB-type structures and deformation twins (DTs). In the ECC image (Fig. 11(a)), the DB is visible as a bright lamella (out-of-Bragg condition) with a thickness of ~ 2 μm. DTs are visible as bright plates with a sharp interface. Fig. 11(c) corresponds to a diffraction pattern taken along the [−1 1 0] zone axis obtained from a region of the interior of the DB, which is indicated by a rectangle in Fig. 11(b). The region also contains a portion of the MB-type structure. No extra diffraction spots are observed in this pattern. On the other hand, Fig. 11(e) shows the corresponding diffraction pattern of the area containing DTs, which is indicated in Fig. 11(d). The diffraction pattern was also taken along the [−1 1 0] zone axis. It corresponds to a twinned diffraction pattern with the twin crystallographic elements $K_1 = \{1\ 1\ 1\}$ (primary twinning plane) and $\eta_1 = \langle 1\ 1\ -2\rangle$ (primary twinning direction). The TEM analysis validates the analysis of the DB, MB, and DT structures performed by ECCI/EBSD and (BF) t-FSEI such as that shown in Fig. 10.

Fig. 12 shows the deformation structure of grains oriented close to <001>//TA directions formed during tensile deformation at −100 °C to $\varepsilon = 0.3$. The deformation structure mainly consists of a fine structure of closely spaced slip bands with an average spacing of 250 nm ± 10 nm (Fig. 12(a)). Under the current channeling conditions, slip bands are imaged as bright thick bands lying parallel to {111} plane traces. With a further decrease of the deformation temperature to −196 °C, the average spacing is reduced to 180 nm ± 10 nm [8]. At these deformation conditions, MBs are observed in the interior of a few grains, Figs. 12(b, c). These deformation structures are formed by thick plates with an average thickness of 500 ± 100 nm that are aligned parallel to {111} plane traces. As reported in a former study [8], the MB structure is further developed with the decrease of the deformation temperature to −196 °C.

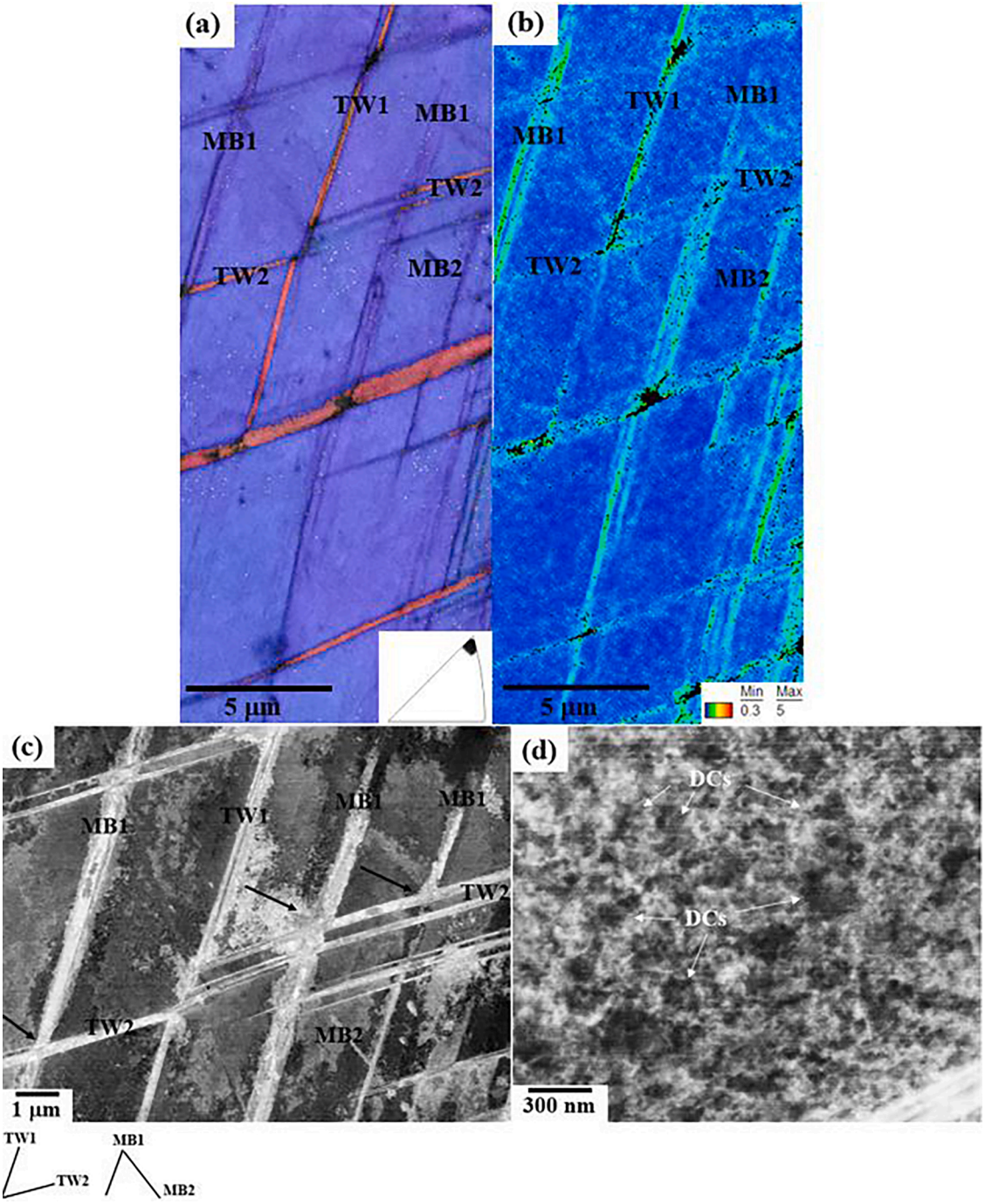

Fig. 7. Room-temperature deformation structure ($\varepsilon = 0.5$) of a grain oriented close to the [7 7 8]//TA direction. (a): IPF-EBSD map; (b): KAM-EBSD map; (c): ECC image of the microband (MB) and twin (TW) structures. Arrows indicate the shearing of MBs by the propagating twins; (d): ECC image of the dislocation cell (DC) structure.

3.3.2. High strain level ($\varepsilon = 0.5 - 0.6$)

With further deformation to $\varepsilon = 0.5 - 0.6$, the main characteristics of the deformation structure formed at cryogenic deformation temperatures are the development of a twin structure in grains that are favorable oriented for deformation twinning, i.e. grains oriented close to <111>// TA and <112>//TA directions (Fig. 13(a)), and the development of a macroscopic deformation structure (deformation band, DB) containing arrays of crystallographic MBs in grains oriented close to <001>//TA directions (Figs. 13(c, d)). Fig. 13(a) shows an example of the twin structure in a grain oriented close to <111>//TA directions formed at −100 °C. Similar to the twin structure reported in austenitic FeMnC TWIP steels and FeMnAlC low-density steels [1,5,54], deformation twins formed at $\varepsilon = 0.5 - 0.6$ are distributed into bundles containing several twins. To estimate the influence of the deformation temperature on the twin structure, we have considered the average twin bundle spacing as the scaling parameter. This parameter was estimated from ECC images of the twin structure formed in grains oriented close to <111>//TA directions. At the deformation temperature of −100 °C, the average twin bundle spacing, λ_{twin}, is reduced from ~ 9.7 ± 0.8 μm ($\varepsilon = 0.3$) to ~ 3.1 ± 0.5 μm ($\varepsilon = 0.5$). Comparatively, the refinement of the twin structure with the strain level at −196 °C is more significant resulting in a finer twin structure, Fig. 13(b). Specifically, λ_{twin} is reduced from ~ 8.2 ± 0.5

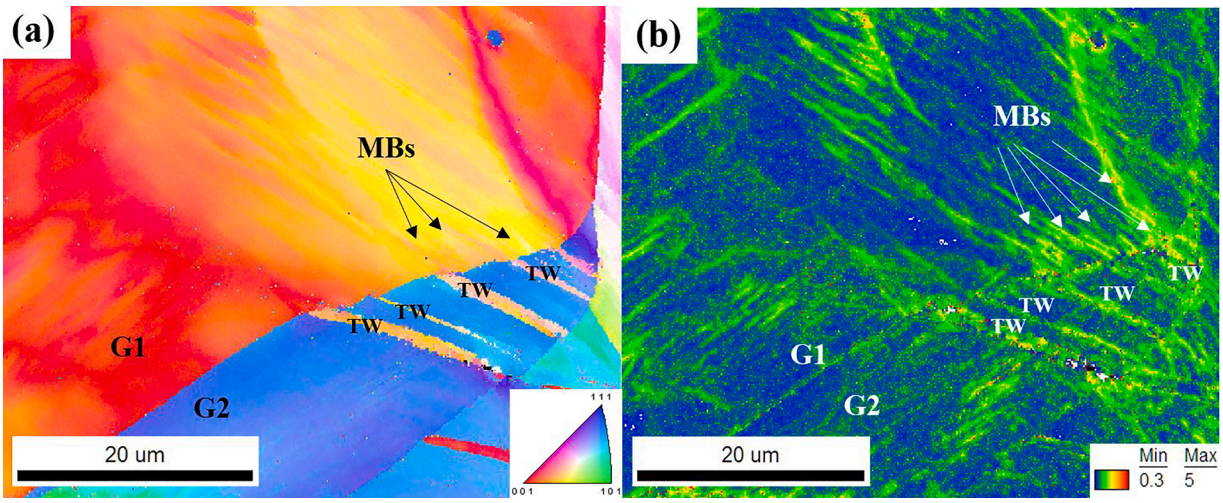

Fig. 8. GB-assisted nucleation of microbands (MBs) in a grain oriented close to the [1 1 28]//TA direction (G1). (a): IPF-EBSD map; (b): KAM-EBSD map. TW: Deformation twins.

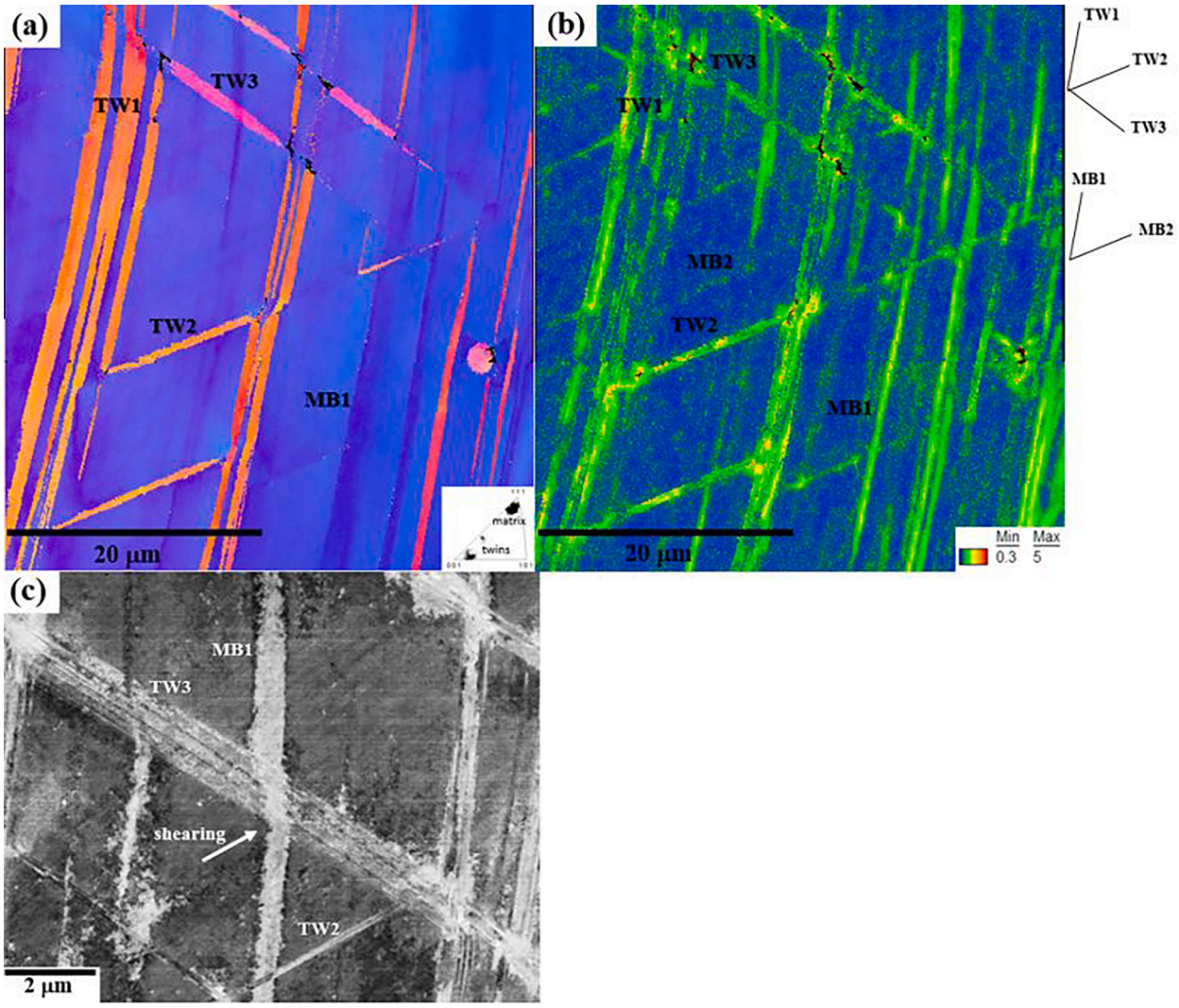

Fig. 9. Deformation structure of a grain oriented close to the [6 5 7]//TA direction after tensile deformation at −100 °C to $\varepsilon = 0.3$. (a): IPF-EBSD map; (b): KAM-EBSD map; (c): ECC image. The arrow indicates the shearing of MBs by the propagating twins. MB: Microband system; TW: twin system.

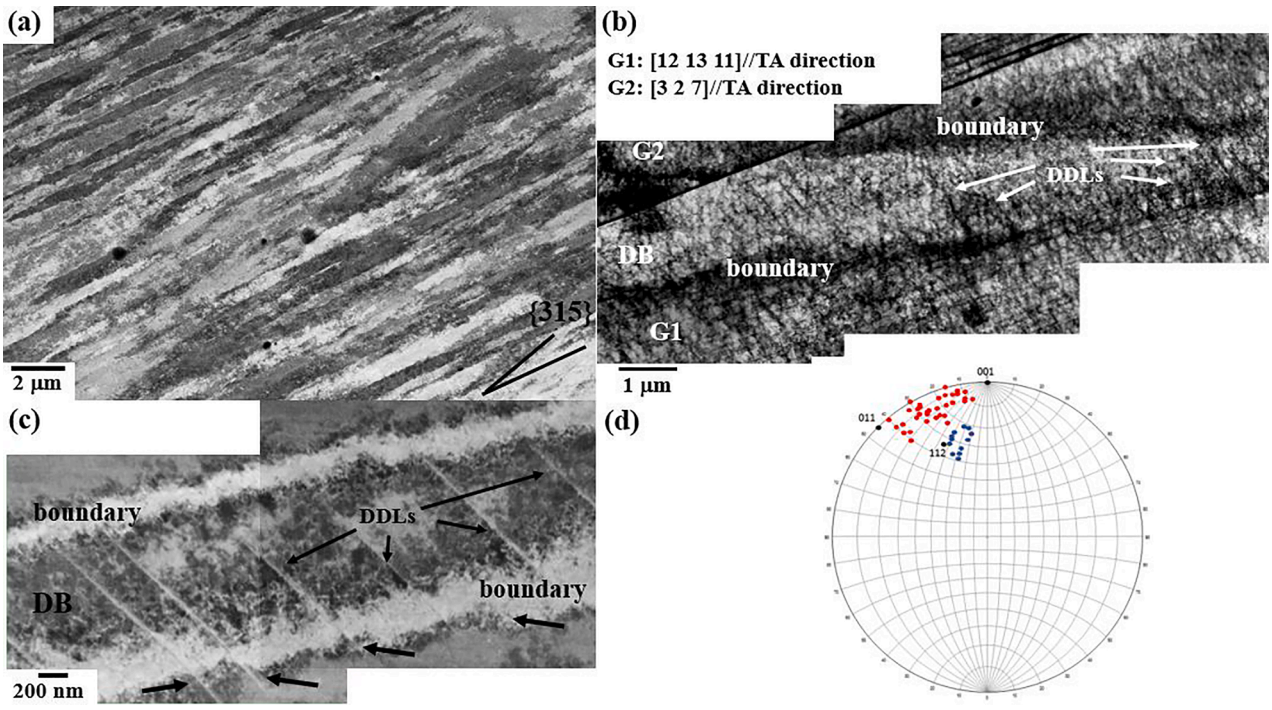

Fig. 10. Deformation structures of grains oriented close to the <112>//TA directions after tensile deformation at −100 °C to $\varepsilon = 0.3$. (a): ECC image of the cell-block structure. (b, c): (BF) t-FSE image and corresponding ECC image of a deformation band (DB). Arrows indicate the shearing of MBs by dense dislocation layers (DDLs). (d): Stereographic projection of the rotation axes for misorientations between points in the interior of the DB and neighboring points of the crystal matrix (red dots) and between points in the boundary of the DB and neighboring points of the crystal matrix (blue dots) calculated from misorientation profiles of lines crossing the DB.

μm ($\varepsilon = 0.3$) to $\lambda_{twin} \sim 2.0 \pm 0.5$ μm ($\varepsilon = 0.5$). Fig. 13(c, d) show an example of the deformation structure associated with strain localization formed at −196 °C in a grain oriented close to <001>//TA directions. The deformation structure is formed by two MB systems (only one MB system is visible in Fig. 13(c)) and two DB systems. The MB system is formed by individual MBs parallel to {111} plane traces. DBs are characterized by several arrays of closely spaced crystallographic MBs, as shown in the ECC image of Fig. 13(d).

4. Discussion

4.1. Deformation behavior

The deformation structure of the Fe-30Mn-6.5Al-0.3C low-density steel deformed at the temperature range 25 °C (RT) to −196 °C is formed by a complex mixture of dislocation and twin structures. Table 2 summarizes the dislocation configurations observed in the present study. The evolving dislocation structure consists of several types of dislocation configurations associated with different types of deformation behavior, namely, homogeneous (e.g. dislocation cells (DCs) and cell blocks (CBs)) and inhomogeneous (microbands (MBs) and deformation bands (DBs)) [55–57]. As shown in Section 4.2, MBs and DBs are associated with strain localization phenomena. Fig. 14 summarizes the scale of the deformation structures formed at the different deformation temperatures. The figure plots the average sizes of dislocation structures associated with homogeneous deformation, i.e. DCs, CB, and slip bands (SBs), and the average spacing of dislocation structures associated with inhomogeneous deformation, i.e. MBs and DBs. At RT deformation conditions, the average size of dislocation configurations associated with homogeneous plasticity is at the nanoscale (~ 200 – 300 nm). The size of these dislocation configurations is determined by the resolved in-grain stress acting on them [58]. These dislocation structures are homogeneously distributed in the interior of the grains as they accommodate the in-grain plastic deformation. On the other hand, the spacing of dislocation structures associated with inhomogeneous plasticity is at the micron scale (~ 5 – 10 μm). This result suggests that the in-grain sources of inhomogeneous plasticity associated with strain localization phenomena (see Section 4.2 for further details) are distributed at the micron scale. Accordingly, the plastic behavior at RT deformation conditions can be considered as a combination of homogeneous and inhomogeneous character. At cryogenic deformation temperatures, the spacing of the dislocation structures associated with inhomogeneous plasticity is significantly reduced, i.e. from 5 - 10 μm at RT to ~ 2.1 μm at −196 °C. This is, the population of in-grain sources of strain localization increases promoting the inhomogeneous character of plastic deformation.

4.2. Dislocation configurations associated with strain localization phenomena

The present study reveals that the formation of dislocation configurations associated with strain localization phenomena, namely MBs and DBs, exhibit strong deformation temperature and grain orientation dependences, as shown in Table 2. MBs are formed in the whole analyzed range of deformation temperature, i.e. from RT to −196 °C. However, DBs are only formed at cryogenic deformation temperatures. In particular, two types of DBs related to different strain localization scales are observed, namely, macro-scale over several grains (Fig. 10(b, c)) and micro-scale through the grain interior (Fig. 13(c)). At the macro-scale, strain localization associated with lattice rotations around [1 1 2]//TA directions is concentrated on the boundaries of the propagating DB. At the micro-scale, strain localization is associated with the formation of in-grain arrays of MBs. Macroscopic DBs associated with intense plastic localization (lattice rotations ~ 25 - 30°) have been reported in austenitic steels deformed to high strain levels [18,59,60] or high-strain rate conditions [61–63]. The macroscopic DBs formed at the current deformation conditions are associated with moderated plastic localization (lattice rotations ~ 2 - 5°).

Fig. 15 plots the crystallographic orientation dependences of the dislocation and twin structures formed at a moderated strain level of $\varepsilon =$

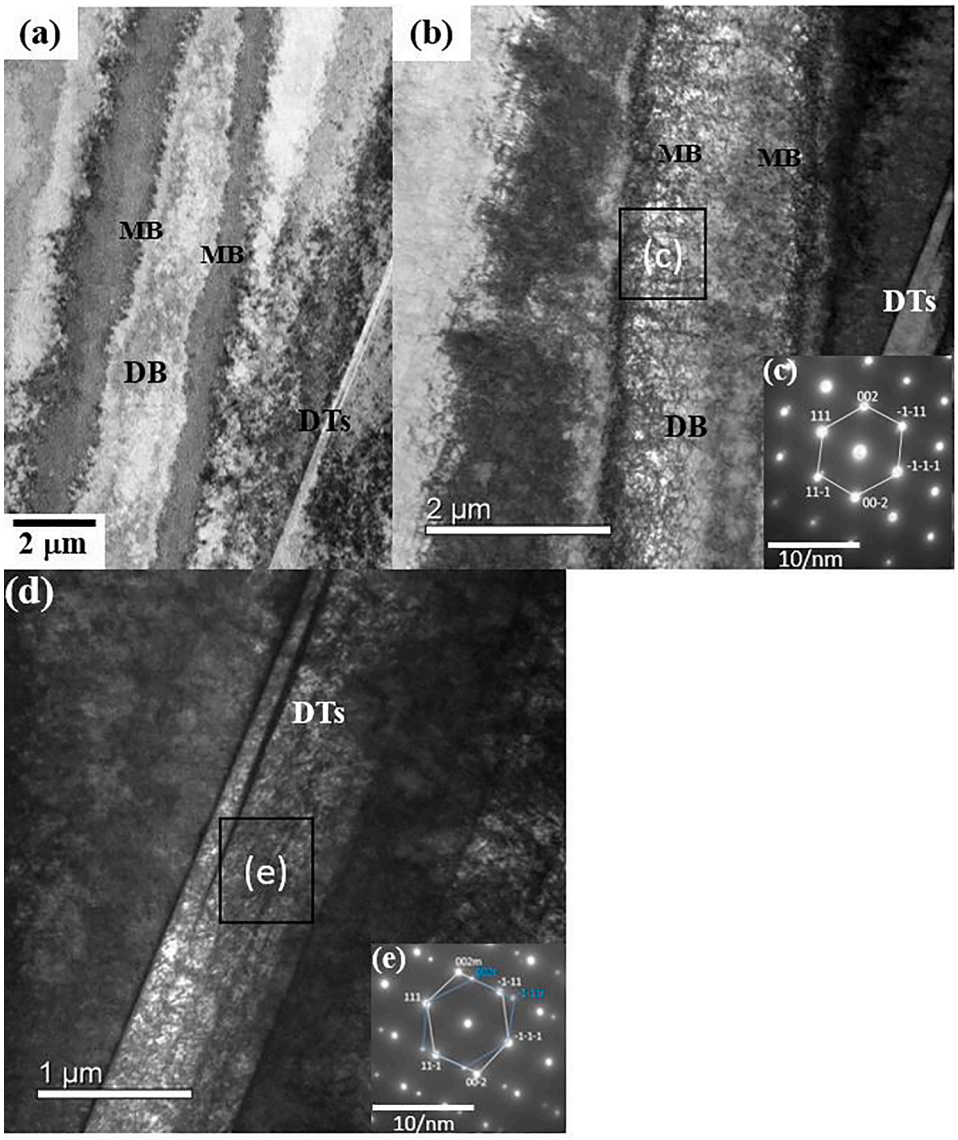

Fig. 11. ECCI and TEM analysis of a region containing a deformation band (DB) delimited by microband (MB)-type structures (b, c) and deformation twins (DTs) (d, e). (a): ECC image; (b, c): TEM analysis of the MB-type structure; (d, e): TEM analysis of the twinned region. The indexes m and t in (e) correspond to the spots of the matrix and DT, respectively.

0.3 for the investigated deformation temperatures. The plotted data are summarized in Table 2. The observed crystallographic orientation dependence of the twin structure is in line with former reports on tensile-deformed austenitic FeMnC twinning-induced plasticity steels [41,64]. Interestingly, the plot shows a strong effect of the deformation temperature on the orientation dependence of the dislocation structure. Specifically, at RT deformation conditions, the MB structure exhibits a strong orientation dependence, i.e. they are mainly formed in grains oriented close to <111>//TA directions. However, at cryogenic deformation conditions, MBs are formed in all the investigated texture components. The observed grain orientation dependence of the MB structure with the deformation temperature can be explained as follows. ECC images of the RT dislocation configuration formed in grains containing MBs reveal the formation of dislocation configurations controlled by the activation of double cross-slip, such as wavy dislocations (Fig. 4), dipoles (Figs. 4 and 5), and DCs (Fig. 7). Dislocation dipoles and multipole configurations have been observed during the early stages of deformation in fcc metals [65–68]. These dislocation configurations are not stable and at a certain stress level are either dissolved [65,69,70] or evolve into dislocation cells and lamellar dislocation configurations [48,50,71]. In this scenario, MB formation is likely to occur by the dislocation cross-slip-assisted approach proposed by Jackson [71,72]. In this model, the avalanche glide of dislocation groups on latent slip planes assisted by double cross-slip results in the formation of multipolar arrays of primary dislocations and prismatic dipoles. The arrays of prismatic loops produce internal stresses that are relaxed by secondary slip resulting in the formation of paired sheet dislocation configurations that evolve into an MB structure. Edge dislocation dipoles such as those shown in Figs. 4b and 5 promote the double cross-slip of the gliding dislocation groups due to the resulting forces acting on them when they interact with edge dipoles. Screw dipole segments are annihilated at the early stages of deformation and hence, play a negligible role in the MB formation process. This model has been experimentally validated in bcc steels highly deformed at RT deformation conditions [24,25,72–75].

Considering that MB formation assisted by cross-slip is favored in grains where dislocation plasticity is concentrated on a few non-coplanar slip systems [74–76], this effect will be enhanced, at tensile deformation conditions, in grains oriented close to <111>//TA directions [77]. This is in line with the observed orientation dependence of MBs found at RT deformation conditions (Fig. 15(a)). At cryogenic

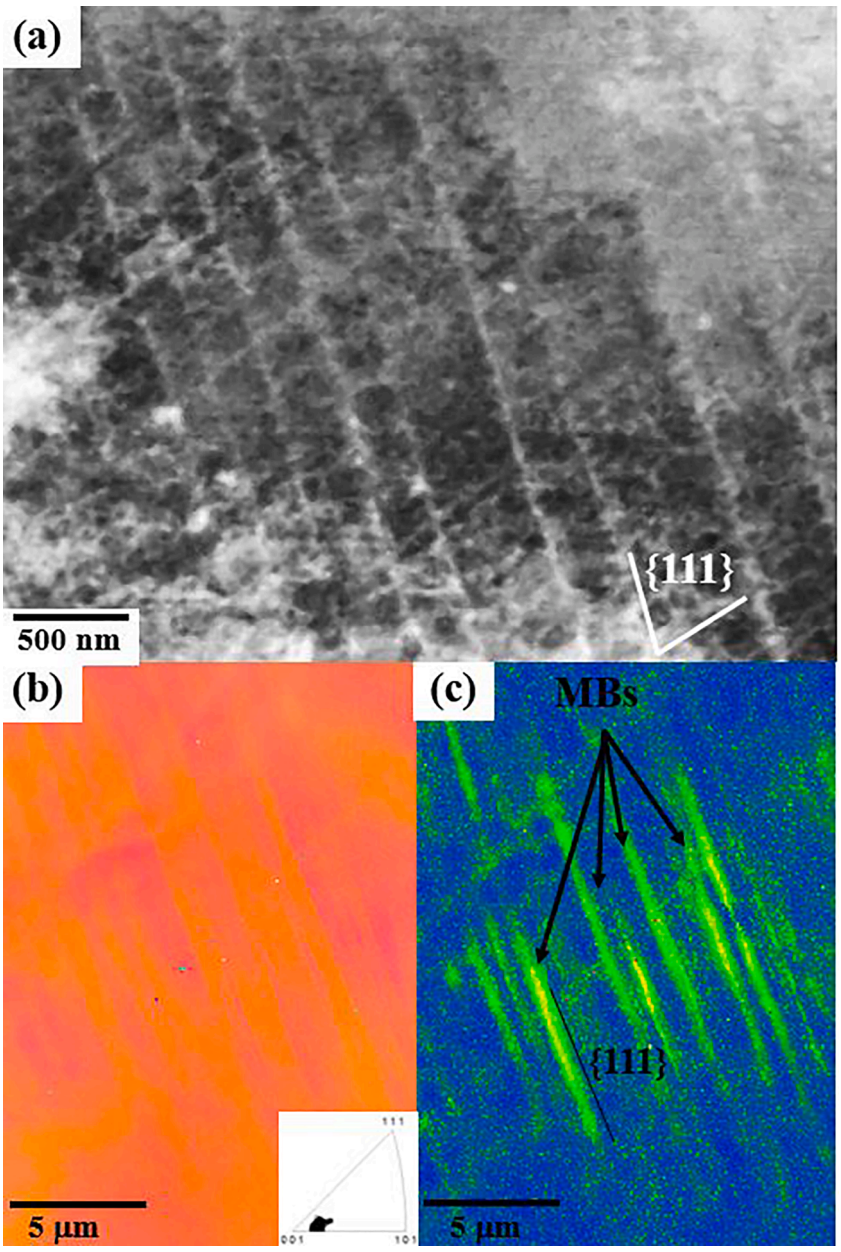

Fig. 12. Deformation structure of grains oriented close to <001>//TA directions after tensile deformation at −100 °C to $\varepsilon = 0.3$. (a): ECC image taken under (0 2 0) channeling conditions with $w >> 0$; (b): IPF-EBSD map; (c): KAM-EBSD map. MBs: Microbands.

deformation conditions, our former study [8] has shown that MB formation is associated with two formation mechanisms occurring in the grain interior (in-grain MB formation) and at grain boundaries (GB-assisted MB formation). The classification is based on the microstructural origin of the stress localization that triggers the plastic localization. In the in-grain MB formation mechanism, MBs are associated with the local concentration of dislocation slip on closely spaced slip bands such as that occurring in the boundaries of the DB shown in Fig. 10(b). This mechanism is grain orientation non-dependent [78], which explains the observed behavior of the MB structure on the grain orientation shown in Figs. 15(b, c). In the GB-assisted mechanism, MB formation is triggered by the stress localization acting at GBs due to the interaction of deformation twins with GBs when propagating through the polycrystalline material. The activation of the GB-assisted mechanism is related to the developed twin structure on neighboring grains, as shown in Fig. 8.

Interestingly, the present study shows that the alignment of MBs formed in grains oriented close to <111>//TA directions during the deformation temperature range 25 °C to −196 °C is non-crystallographic, i.e. they are aligned along {315} plane traces. This result indicates that the specific dislocation-based mechanism that controls the MB nucleation process has no influence on the alignment of the dislocation structure upon deformation. This is in line with former studies showing that the alignment of dislocation structures delimited by geometrically necessary boundaries (GNBs) in fcc metals is associated with the lattice rotations accommodated by the active slip systems [55, 79–81]. In particular, the observed alignment of the MB structure in this study agrees with that predicted by Winther's model [77]. According to this model, these dislocation structures are formed in grains containing four slip systems in two non-coplanar slip planes that account for 80 – 90 % of the total dislocation slip, i.e. grains oriented close to <111>//TA directions.

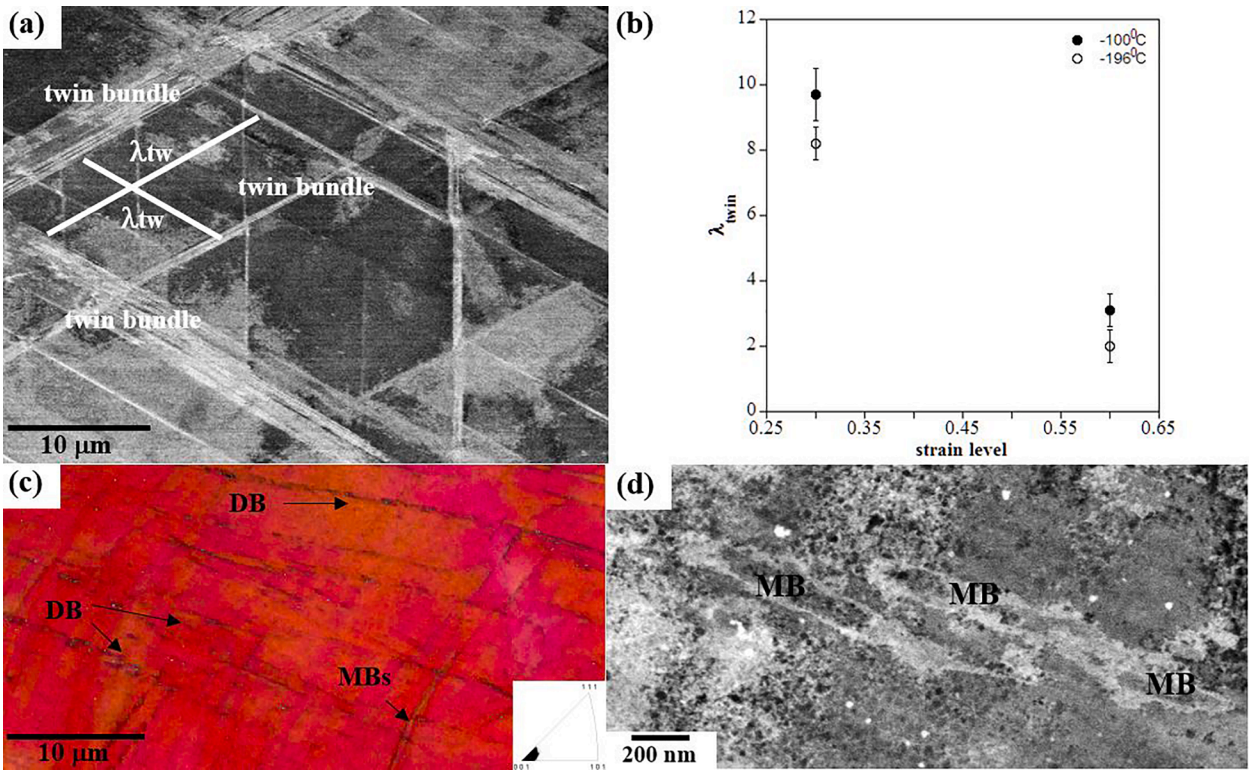

Fig. 13. (a): Twin structure formed at −100 °C ($\varepsilon = 0.5$) in a grain oriented close to <111>//TA directions. (b): Variation of the twin bundle spacing, λ_{twin}, with the deformation temperature and strain level in grains oriented close to <111>//TA directions. (c, d): IPF-EBSD map of the deformation band (DB) and microband (MB) structures formed at −196 °C ($\varepsilon = 0.5$) in a grain oriented close to <001>//TA directions. (d): ECC image of the MB structure.

Table 2
Dislocation configurations formed in a Fe-30Mn-0.6Al-0.3C low-density steel deformed at room temperature (RT), −100 °C, and −196 °C to strain levels of ε = 0.3 and ε = 0.5 −0.6. TA: Tensile axis; CBs: Cell blocks; DCs: Dislocation cells; MBs: Microbands; DBs: Deformation bands.

Dislocation configuration	ε = 0.3			ε = 0.5 - 0.6		
	RT	−100 °C	−196 °C	RT	−100 °C	−196 °C
Edge dipole bundles	<111>//TA <001>//TA	——-	——-	——-	——-	——-
CBs	<112>//TA	<112>//TA	<112>//TA	<112>//TA	<112>//TA	——-
DCs	<001>//TA	——-	——-	<001>//TA <111>//TA	——-	——-
MBs	<111>//TA	<111>//TA GB-assisted	<111>//TA <001>//TA GB-assisted	<111>//TA GB-assisted	<111>//TA <001>//TA GB-assisted	<001>//TA GB-assisted
DBs		<112>//TA	<112>//TA		<112>//TA	<112>//TA<001>//TA

4.3. *Strain-hardening behavior. Effect of strain localization*

Fig. 16 shows the strain hardening rate against the true strain of the tensile deformed materials at the deformation temperatures of 25 °C (RT), −100 °C, and −196 °C. It can be seen that the deformation temperature strongly influences the strain-hardening behavior. Specifically, six different hardening stages (A, B, C, D, E, and F) are distinguished in the evolution of the strain hardening rate with the true stress. It should be pointed out that the labeling of the hardening stages used in this work must not be confused with the classical hardening stage analysis used for single crystals and polycrystals of face-centered metals (fcc) metals [58, 82]. The first stage (stage A) is similar to the stage III hardening regime of fcc metals containing a high stacking fault energy [58,82] and is characterized by a continuous decrease of the strain hardening rate. Stage B is characterized by a constant hardening rate, which indicates the activation of a strain-hardening mechanism. At RT deformation conditions, it is associated with dislocation structure hardening. At cryogenic deformation conditions, the activation of twinning results in a further decrease of the dislocation mean free path and hence, higher hardening. However, this effect is moderated due to the large average twin spacing (the average twin bundle spacing is ~ 8 - 10 μm, Fig. 12 (b)). With further straining at RT, the strain hardening rate increases gradually reaching a plateau at $\varepsilon = 0.19$ (Stage C) and subsequently decreases until rupture (stage D). Upon deformation at cryogenic temperatures, the strain-hardening curves do not exhibit the hardening stage C. Two strain-hardening behaviors are instead observed. At the deformation temperature of −100 °C, the strain hardening rate steadily decreases until fracture at a similar rate to that occurring at RT deformation conditions. This result indicates that the contribution of twinning to the hardening of stage D is limited. At the deformation temperature of −196 °C, the strain hardening extends significantly further than that at −100 °C due to the activation of an extended hardening stage, namely, stage E. This hardening stage is associated with the further refinement of the dislocation mean free path due to the activation of secondary twinning. Finally, with further straining, the strain hardening rate decreases until rupture (stage F).

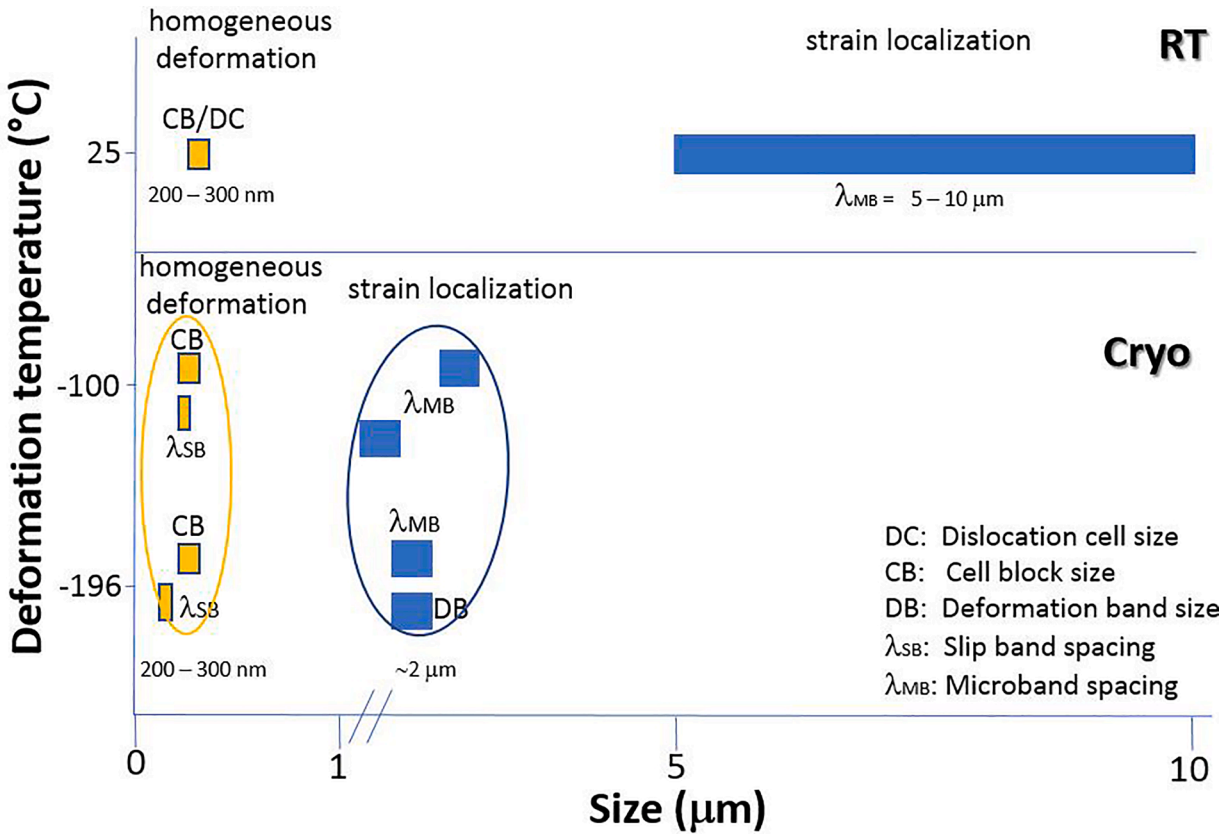

Fig. 14. Evolution of the size/spacing of the analyzed dislocation structures with the deformation temperature.

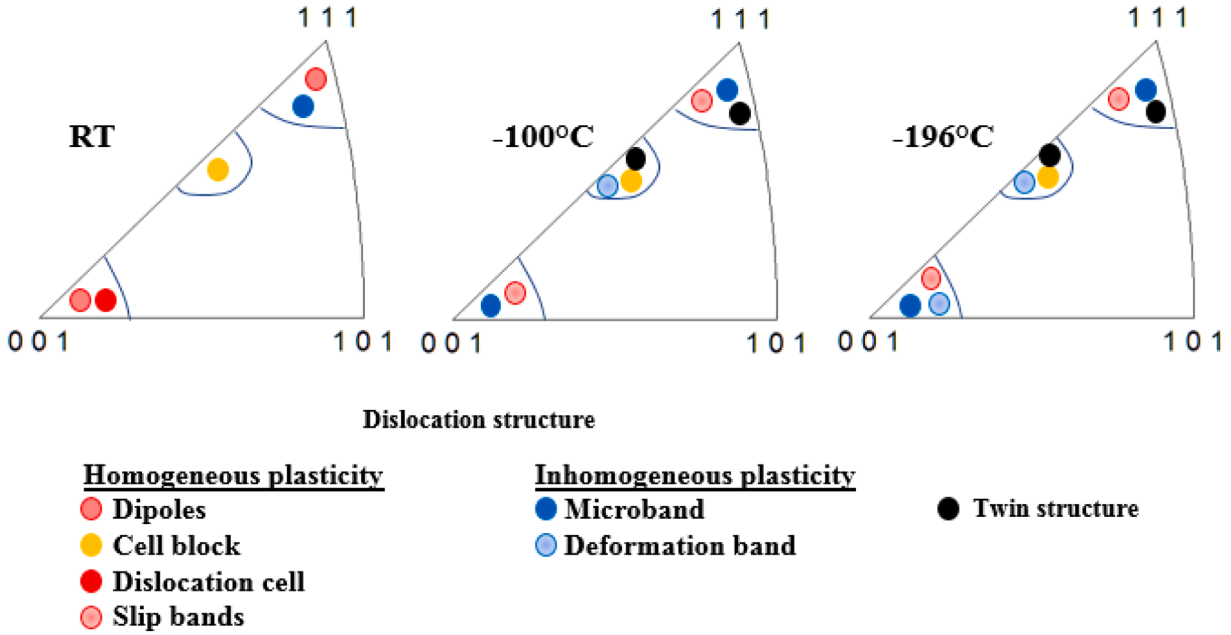

Fig. 15. Crystallographic orientation dependence of the dislocation and twin structures formed at $\varepsilon = 0.3$ for the deformation temperatures 25 °C (RT) (a), −100 °C (b), and −196 °C (c). Data from Table 2.

The analysis of the strain-hardening behavior indicates that the main effect of the deformation temperature on the strain-hardening behavior is the activation of deformation twinning. This effect results in the extension of stage B at $\varepsilon \sim 0.1$ and at the deformation temperature of −196 °C, the activation of stage E at $\varepsilon \sim 0.35$ that provides further strain-hardening capacity to the material. Regarding the contribution of dislocation structures associated with strain localization phenomena to the strain-hardening behavior, it is still a controversial issue as the contribution of MBs to the strain-hardening has not been yet experimentally clarified [1–3,6,7,9–11,13]. In the present study, ECC images reveal thatat cryogenic deformation conditions, MBs and DBs offer a relatively small mechanical resistance against the advance of

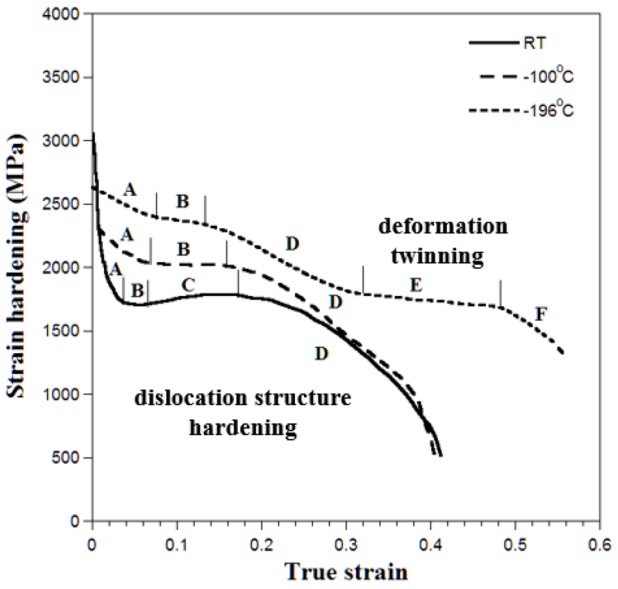

Fig. 16. Strain-hardening curves of the Fe-30Mn-6.5Al-0.3C low-density steel tensile deformed at the deformation temperatures of 25 °C (RT), −100 °C, and −196 °C.

deformation twins and dense dislocation layers (DDLs) through them (Figs. 7(c), 9(c), 10(b, c)). As a former study shows [54], the mechanical strength of a deformation twin, which is provided by the local Peach-Koehler force created by the trailing partial of the twin dislocation that forms the twin tip, is too high to be overcome by the stress field of a dislocation structure such as DCs, MBs and DBs. On the other hand, the small mechanical resistance offered by the boundaries of MBs and DBs to the propagation of DDLs is associated with the high shear stress of the dislocation array, σ_{xy}^{DDL}, that scales with the inverse of the dislocation spacing, h, as follows [83,84]:

$$\sigma_{xy}^{DDL} \sim GbN \Big/ [(N-1)\,\pi(1-\nu)h] \quad (1)$$

where G is the shear modulus, b is the Burgers vector, ν is the Poisson ratio, N is the number of dislocations, and h is the dislocation spacing.

These results indicate that dislocation configurations associated with strain localization phenomena are weak obstacles to the propagation of dislocation configurations formed by arrays of small spaced dislocations i.e. planar dislocation structures. Accordingly, the contribution of MBs to the strain-hardening behavior at cryogenic deformation conditions is negligible. At RT deformation conditions, the small overall MB population results in a negligible contribution of MB-dislocation interactions to the overall strain-hardening. This analysis suggests that MBs play a small role in the hardening of the Fe-30Mn-6.5Al-0.3C low-density steel upon the investigated deformation range, which agrees with former studies in austenitic multicomponent alloys [1,10,11,13]. As KAM-EBSD maps reveal, dislocation structures associated with strain localization accommodate a high level of geometrically necessary dislocations, which could enhance the plastic behavior and hence, ductility. However, in the present study, the increase of the MB population by decreasing the deformation temperature from RT to −100 °C (Fig. 13) has no visible influence on the ductility. It can, however, be expected that when the contribution of MBs to the plastic accommodation is significant, they could enhance the ductility resulting in the MBIP effect. At the moment, there is no experimental evidence that validates this effect. Further work is needed to evaluate the role of the dislocation structures associated with strain localization phenomena that promote the ductilization of austenitic FeMnAlC low-density steels.

5. Conclusions

We have investigated the influence of the deformation temperature from 25 °C (RT) to −196 °C on the dislocation structures associated with strain localization phenomena in an austenitic Fe-30Mn-6.5Al-0.3C (wt. %) low-density steel by combined electron channeling contrast imaging (ECCI) and electron backscatter diffraction (EBSD) techniques. The main characteristics of the dislocation structures were evaluated on the main texture components, i.e. <111>//tensile axis, <112>//tensile axis, and <001>//tensile axis directions. The following conclusions can be drawn:

-The deformation temperature has a strong influence on the deformation behavior. Cryogenic deformation temperatures promote the inhomogeneous character of the plastic behavior due to the enhanced formation of dislocation structures associated with strain localization, namely microbands (MBs) and deformation bands (DBs). These dislocation structures are associated with different strain localization scales, i.e. micro-scale and macro-scale, respectively.

-The deformation temperature has a strong influence on the thermal-assisted dislocation processes controlling the formation of MBs. ECCI analysis of the dislocation structures formed in the surroundings of MBs suggests that MB formation at RT deformation conditions is controlled by the dislocation cross-slip-assisted model proposed by Jackson [71,72]. At cryogenic deformation temperatures, MB formation is associated with localized planar slip phenomena acting on closely spaced slip bands. This variation in the dislocation processes controlling the formation of MBs has a profound effect on the grain orientation dependence of the MB structure but not on its crystallographic alignment.

-Cryogenic deformation temperatures enhance strain-hardening due to the activation of deformation twinning. This effect results in the extension of hardening stage B at $\varepsilon \sim 0.1$, and at the deformation temperature of −196 °C, the activation of a further hardening stage (stage E) at $\varepsilon \sim 0.35$ that provides further strain-hardening capacity to the material. This effect is associated with the reduction of the γ_{SFE} at cryogenic temperatures.

-We find that dislocation structures associated with strain localization (MBs and DBs) have a small contribution to the strain-hardening and ductility. These effects are ascribed to the small mechanical resistance of these dislocation structures against the advance of twin boundaries and dense dislocation layers (DDLs), and the comparatively small plastic strain accommodated by them, respectively.

Declaration of Competing Interest

The authors declare that they have no known competing financial interests or personal relationships that could have appeared to influence the work reported in this paper.

References

[1] I. Gutierrez-Urrutia, D. Raabe, Multistage strain hardening through dislocation substructure and twinning in a high strength and ductile weight-reduced Fe-Mn-Al-C steel, Acta Mater. 60 (2012) 5791–5802.
[2] J.D. Yoo, K.T. Park, Microband-induced plasticity in a high Mn–Al–C light steel, Mater. Sci. Eng. A 496 (2008) 417–424.
[3] J.D. Yoo, S.W. Hwang, K.T. Park, Origin of extended tensile ductility of a Fe-28Mn-10Al-1C steel, metall, Mater. Trans. A (2009) 1520–1523, 40A.
[4] K.T. Park, G. Kim, S.K. Kim, S.W. Lee, S.W. Hwang, C.S. Lee, On the transitions of deformation modes of fully austenitic steels at room temperature, Met. Mater. Int. 16 (2010) 1–6.
[5] I. Gutierrez-Urrutia, Low Density Fe–Mn–Al–C steels: phase structures, Mech.Prop. ISIJ Int 61 (2021) 16–25.
[6] J. Moon, S.J. Park, J.H. Jang, T.H. Lee, C.H. Lee, H.U. Hong, H.N. Han, J. Lee, B. H. Lee, C. Lee, Investigations of the microstructure evolution and tensile deformation behavior of austenitic Fe-Mn-Al-C lightweight steels and the effect of Mo addition, Acta Mater. 147 (2018) 226–235.
[7] C. Li, K. Li, J. Dong, J. Wang, Z. Shao, Mechanical behaviour and microstructure of Fe-20/27Mn–4Al-0.3C low magnetic steel at room and cryogenic temperatures, Mater. Sci. Eng. A 809 (2021), 140998.
[8] I. Gutierrez-Urrutia, A. Shibata, K. Tsuzaki, Microstructural study of microbands in a Fe-30Mn-6.5Al-0.3C low-density steel deformed at cryogenic temperature by

combined electron channeling contrast imaging and electron backscatter diffraction, Acta Mater. 233 (2022), 117980.
[9] H. Zhi, J. Li, W. Li, M. Elkot, S. Antonov, H. Zhang, M. Lai, Simultaneously enhancing strength-ductility synergy and strain hardenability via Si-alloying in medium-Al FeMnAlC lightweight steels, Acta Mater. 245 (2023), 118611.
[10] Z. Wang, I. Baker, Z. Cai, S. Chen, J.D. Poplawsky, W. Guo, The effect of interstitial carbon on the mechanical properties and dislocation substructure evolution in Fe40.4Ni11.3Mn34.8Al7.5Cr6 high entropy alloys, Acta Mater. 120 (2016) 228–239.
[11] Z. Wang, I. Baker, W. Guo, J.D. Poplawsky, The effect of carbon on the microstructures, mechanical properties, and deformation mechanisms of thermo-mechanically treated Fe40.4Ni11.3Mn34.8Al7.5Cr6 high entropy alloys, Acta Mater. 126 (2017) 346–360.
[12] X. Liu, Y. Wu, Y. Wang, J. Chen, R. Bai, L. Gao, Z. Xu, W.Y. Wang, C. Tan, X. Hui, Enhanced dynamic deformability and strengthening effect via twinning and microbanding in high density NiCoFeCrMoW high-entropy alloys, J. Mater. Sci. Tech. 127 (2022) 164–176.
[13] D.L. Foley, S.H. Huang, E. Anber, L. Shanahan, Y. Shen, A.C. Lang, C.M. Barr, D. Spearot, L. Lamberson, M.L. Taheri, Simultaneous twinning and microband formation under dynamic compression in a high entropy alloy with a complex energetic landscape, Acta Mater. 200 (2020) 1–11.
[14] F. Xiong, R. Fu, Y. Li, B. Xu, X. Qi, Influences of nitrogen alloying on microstructural evolution and tensile properties of CoCrFeMnNi high-entropy alloy treated by cold-rolling and subsequent annealing, Mater. Sci. Eng. A 787 (2020), 139472.
[15] D. Peirce, R.J. Asaro, A. Needleman, Overview N°32. Material rate dependence and localized deformation in crystalline solids, Acta Metall. 31 (1983) 1951–1976.
[16] H. Paul, J.H. Driver, Z. Jasienski, Shear banding and recrystallization nucleation in a Cu–2%Al alloy single crystal, Acta Mater. 50 (2002) 815–830.
[17] J. Hirsch, K. Lücke, N.°.7.6. Overview, Mechanism of deformation and development of rolling textures in polycrystalline F.C.C. metals-I. Description of rolling texture development in homogeneous CuZn alloys, Acta Metall. 36 (1988) 2863–2882.
[18] C. Donadille, R. Valle, P. Dervin, R. Penelle, Overview No 82. Development of texture and microstructure during cold-rolling and annealing of F.C.C. alloys: example of an austenitic stainless steel, Acta Metall. 37 (1989) 1547–1571.
[19] D.G. Ulmer, C.J. Altstetter, Hydrogen-induced strain localization and failure of austenitic stainless steels at high hydrogen concentrations, Acta Metall. Mater. 39 (1991) 1237–1248.
[20] E.H. Lee, T.S. Byun, J.D. Hunn, M.H. Yoo, K. Farrell, L.K. Mansur, On the origin of deformation microstructures in austenitic stainless steel: part I-Microstructures, Acta Mater. 49 (2001) 3269–3276.
[21] T.S. Byun, E.H. Lee, J.D. Dunn, Plastic deformation in 316LN stainless steel - Characterization of deformation microstructures, J. Nuclear Mater. 321 (2003) 29–39.
[22] D.P. Abraham, C.J. Altsetter, Hydrogen-enhanced localization of plasticity in an austenitic stainless steel, Metall. Mater. Trans. A 26 (1995) 2859–2871.
[23] I. Aubert, J.M. Olive, N. Saintier, The effect of internal hydrogen on surface slip localisation on polycrystalline AISI 316L stainless steel, Mater. Sci. Eng. A 527 (2010) 5858–5866.
[24] E.F. Rauch, J.H. Schmitt, Dislocation substructures in mild steel deformed in simple shear, Mater. Sci. Eng. A 113 (1989) 441–448.
[25] S. Thuillier, E.F. Rauch, Development of microbands in mild steel during cross loading, Acta Metall. Mater. 42 (1994) 1973–1983.
[26] H. Kim, D.W. Suh, N.J. Kim, Fe–Al–Mn–C lightweight structural alloys: a review on the microstructures and mechanical properties, Sci. Technol. Adv. Mater. 14 (2013), 014205.
[27] R. Rana, C. Lahaye, R.K. Ray, Overview of lightweight ferrous materials: strategies and promises, JOM 66 (2014-R) 1734–1746.
[28] I. Gutierrez-Urrutia, S. Zaefferer, D. Raabe, Electron channeling contrast imaging of twins and dislocations in twinning-induced plasticity steels under controlled diffraction conditions in a scanning electron microscope, Scripta Mater 61 (2009) 737–740.
[29] I. Gutierrez-Urrutia, S. Zaefferer, D. Raabe, Coupling of electron channeling with EBSD: toward the quantitative characterization of deformation structures in the SEM, JOM 65 (2013) 1229–1236.
[30] I. Gutierrez-Urrutia, Quantitative analysis of electron channeling contrast of dislocations, UltramicroscopyUltramicroscopy 206 (2019), 112826.
[31] I. Gutierrez-Urrutia, A. Shibata, Influence of microscope settings on dislocation imaging in transmission forescattered electron imaging (t-FSEI), Mater. Charact. 203 (2023), 113147.
[32] K.T. Luo, P.W. Kao, D. Gan, Low temperature mechanical properties of Fe-28Mn-5Al-1C alloy, Mater. Sci. Eng. A 151 (1992) L15–L18.
[33] S.S. Sohn, S. Hong, J. Lee, B.C. Suh, S.K. Kim, B.J. Lee, N.J. Kim, S. Lee, Effects of Mn and Al contents on cryogenic-temperature tensile and Charpy impact properties in four austenitic high-Mn steels, Acta Mater. 100 (2015) 39–52.
[34] I. Gutierrez-Urrutia, D. Raabe, Dislocation density measurement by electron channeling contrast imaging in a scanning electron microscope, Scripta Mater 66 (2012) 343–346.
[35] I. Gutierrez-Urrutia, Analysis of FIB induced damage by Electron Channeling Contrast Imaging in the SEM, J. Micros. 265 (2017) 51–59.
[36] J.P. Spencer, C.J. Humphreys, P.B. Hirsch, A dynamical theory for the contrast of perfect and imperfect crystals in the scanning electron microscope using backscattered electrons, Phil. Mag 26 (1972) 193–213.
[37] I. Gutierrez-Urrutia, Analysis of electron channeling contrast of stacking faults in fcc materials, Micros. Microanal. 27 (2021) 318–325.
[38] R. Zauter, F. Petry, M. Bayerlein, C. Sommer, H.J. Christ, H. Mughrabi, Electron channelling contrast as a supplementary method for microstructural investigations in deformed metals, Phil. Mag A 66 (1992) 425–436.
[39] S.L. Dudarev, J. Ahmed, P.B. Hirsch, A.J. Wilkinson, Decoherence in electron backscattering by kinked dislocations, Acta Cryst. A55 (1999) 234–245.
[40] T. Zhai, J.W. Martin, G.A.D. Briggs, A.J. Wilkinson, Fatigue damage at room temperature in aluminium single crystals-III. Lattice rotation, Acta Mater. 44 (1996) 3477–3488.
[41] I. Gutierrez-Urrutia, S. Zaefferer, D. Raabe, The effect of grain size and grain orientation on deformation twinning in a Fe–22wt.% Mn–0.6wt.% C TWIP steel, Mater. Sci. Eng. A 527 (2010) 3552–3560.
[42] S. Allain, J.P. Chateau, O. Bouaziz, S. Migot, N. Guelton, Correlations between the calculated stacking fault energy and the plasticity mechanisms in Fe–Mn–C alloys, Mater. Sci. Eng. A 387-389 (2004) 158–162.
[43] A. Dumay, J.P. Chateau, S. Allain, S. Migot, O. Bouaziz, Influence of addition elements on the stacking-fault energy and mechanical properties of an austenitic Fe–Mn–C steel, Mater. Sci. Eng. A 483-484 (2008) 184–187.
[44] S. Curtze, V.T. Kuokkala, Dependence of tensile deformation behavior of TWIP steels on stacking fault energy, temperature and strain rate, Acta Mater. 58 (2010) 5129–5141.
[45] J.E. Jin, Y.K. Lee, Effects of Al on microstructure and tensile properties of C-bearing high Mn TWIP steel, Acta Mater. 60 (2012) 1680–1688.
[46] J. Nakano, P.J. Jacques, Effects of the thermodynamic parameters of the hcp phase on the stacking fault energy calculations in the Fe-Mn and Fe-Mn-C systems, Calphad 34 (2010) 167–175.
[47] A. Saeed-Akbari, J. Imlau, U. Prahl, W. Bleck, Derivation and variation in composition-dependent stacking fault energy maps based on subregular solution model in high-manganese steels, Metall. Mater. Trans. A 40A (2009) 3076–3090.
[48] D. Kuhlmann-Wilsdorf, N.R. Comins, Dislocation cell formation and work hardening in the unidirectional glide of F.C.C. metals I: basic theoretical analysis of cell walls parallel to the primary glide plane in early stage II, Mater. Sci. Eng. 60 (1983) 7–24.
[49] D. Kuhlmann-Wilsdorf, Theory of plastic deformation:-properties of low energy dislocation structures, Mater. Sci. Eng. A 113 (1989) 1–41.
[50] P.J. Jackson, D. Kuhlmann-Wilsdorf, Low-energy dislocation cell structures produced by cross-slip, Scripta Metall 16 (1982) 105–107.
[51] T. Leffers, R.K. Ray, The brass-type texture and its deviation from the copper-type texture, Prog. Mater. Sci. 54 (2009) 351–396.
[52] H. Paul, A. Morawiec, E. Bouzy, J.J. Fundenberger, A. Piatkowski, Brass-type shear bands and their influence on texture formation, Metall. Mater. Trans. A 35A (2004) 3775–3786.
[53] H. Paul, J.H. Driver, C. Maurice, A. Piatkowski, The role of shear banding on deformation texture in low stacking fault energy metals as characterized on model Ag crystals, Acta Mater. 55 (2007) 575–588.
[54] I. Gutierrez-Urrutia, D. Raabe, Dislocation and twin substructure evolution during strain hardening of an Fe–22wt.% Mn–0.6wt.% C TWIP steel observed by electron channeling contrast imaging, Acta Mater. 59 (2011) 6449–6462.
[55] X. Huang, Grain orientation effect on microstructure in tensile strained copper, Scripta Mater 38 (1998) 1697–1703.
[56] N. Hansen, X. Huang, W. Pantleon, G. Winther, Grain orientation and dislocation patterns, Phil. Mag. 86 (2006) 3981–3994.
[57] X. Huang, G. Winther, Dislocation structures. Part I. Grain orientation dependence, Phil. Mag. 87 (33) (2007) 5189–5214.
[58] U.F. Kocks, H. Mecking, Physics and phenomenology of strain hardening: the FCC case, Prog. Mater. Sci. 48 (2003) 171–273.
[59] Q. Xue, E.K. Cerreta, G.T. Gray III, Microstructural characteristics of post-shear localization in cold-rolled 316L stainless steel, Acta Mater. 55 (2007) 691–704.
[60] C. Zhang, D. Juul Jensen, T. Yu, Microstructure and texture evolution during cold rolling of 316L stainless steel, Metall. Mater. Trans. A 52 (2021) 4100–4111.
[61] H. Berns, V. Gavriljuk, S. Riedner, High Interstitial Stainless Austenitic Steels, Springer, 2013.
[62] K.M. Cho, S. Lee, S.R. Nutt, J. Duffy, Adiabatic shear band formation during dynamic torsional defromation of an HY-100 steel, Acta Metall. Mater. 41 (1993) 923–932.
[63] M.A. Meyers, Y.B. Xu, Q. Xue, M.T. Pérez-Prado, T.R. McNelley, Microstructural evolution in adiabatic shear localization in stainless steel, Acta Mater. 51 (2003) 1307–1325.
[64] B.C.D. Cooman, Y. Estrin, S.K. Kim, Twinning-induced plasticity (TWIP) steels, Acta Mater. 142 (2018) 283–362.
[65] C.S. Pande, P.M. Hazzledine, Dislocation arrays in Cu-Al alloys, I Phil. Mag. 24 (1971) 1039–1057.
[66] V. Gerold, H.P. Karnthaler, On the origin of planar slip in F.C.C. alloys, Acta Metall. 37 (1989) 2177–2183.
[67] A.S. Tetelman, Dislocation dipole formation in deformed crystals, Acta Metall. 10 (1962) 813–820.
[68] P. Veyssière, Y.L. Chiu, Equilibrium and passing properties of dislocation dipoles, Phil. Mag. 87 (2007) 3351–3372.
[69] H. Wang, D.S. Xu, R. Yang, P. Veyssiere, The transformation of narrow dislocation dipoles in selected fcc metals and in g-TiAl, Acta Mater. 57 (2009) 3725–3737.
[70] S.I. Rao, D.M. Dimiduk, J.A. El-Awady, T.A. Parthasarathy, M.D. Uchic, C. Woodward, Screw dislocation cross slip at cross-slip plane jogs and screw dipole annihilation in FCC Cu and Ni investigated via atomistic simulations, Acta Mater. 101 (2015) 10–15.
[71] P.J. Jackson, Dislocation modelling of shear in F.C.C. crystals, Prog. Mater. Sci. 29 (1985) 139–175.

[72] P.J. Jackson, The formation of microbands by cross-slip, Scripta Metall 17 (1983) 199–202.
[73] A. Korbel, P. Martin, Microstructural events of macroscopic strain localization in prestrained tensile specimens, Acta Metall. 36 (1988) 2575–2586.
[74] Q.Z. Chen, A.H.W. Ngan, B.J. Duggan, Microstructure evolution in an interstitial-free steel during cold rolling at low strain levels, Proc. R. Soc. Lond 459 (2003) 1661–1685. A.
[75] K. Shen, B.J. Duggan, Microbands and crystal orientation metastability in cold rolled interstitial-free steel, Acta Mater. 55 (2007) 1137–1144.
[76] Q.Z. Chen, B.J. Duggan, On cells and microbands formed in an interstitial-free steel during cold rolling at low to medium reductions, Metall. Mater. Trans. A 35A (2004) 3423–3430.
[77] G. Winther, Slip systems extracted from lattice rotations and dislocation structures, Acta Mater. 56 (2008) 1919–1932.
[78] J.C. Huang, G.T.Gray III, Microband formation in shock-loaded and quasi-statically deformed metals, Acta Metall. 37 (1989) 3335–3347.
[79] G. Winther, X. Huang, N. Hansen, Crystallographic and macroscopic orientation of planar dislocation boundaries-Correlation with grain orientation, Acta Mater. 48 (2000) 2187–2198.
[80] X. Huang, N. Hansen, Grain orientation dependence of microstructure in aluminium deformed in tension, Scripta Mater 37 (1997) 1–7.
[81] G. Winther, D.J. Jensen, N. Hansen, Dense dislocations walls and microbands aligned with slip planes. theoretical considerations, Acta Mater. 45 (1997) 5059–5068.
[82] E. Nes, Modelling of work hardening and stress saturation in FCC metals, Prog. Mater. Sci. 41 (1998) 129–193.
[83] J.P. Hirth, J. Lothe, Theory of Dislocations, 2nd ed., John Wiley & Sons, 1982.
[84] C.S. Pande, Dislocation pile-ups and passing stresses, Phil. Mag. 21 (169) (1970) 195–202.